Cell Reports

Article

MutSβ regulates G4-associated telomeric R-loops to maintain telomere integrity in ALT cancer cells

Graphical abstract

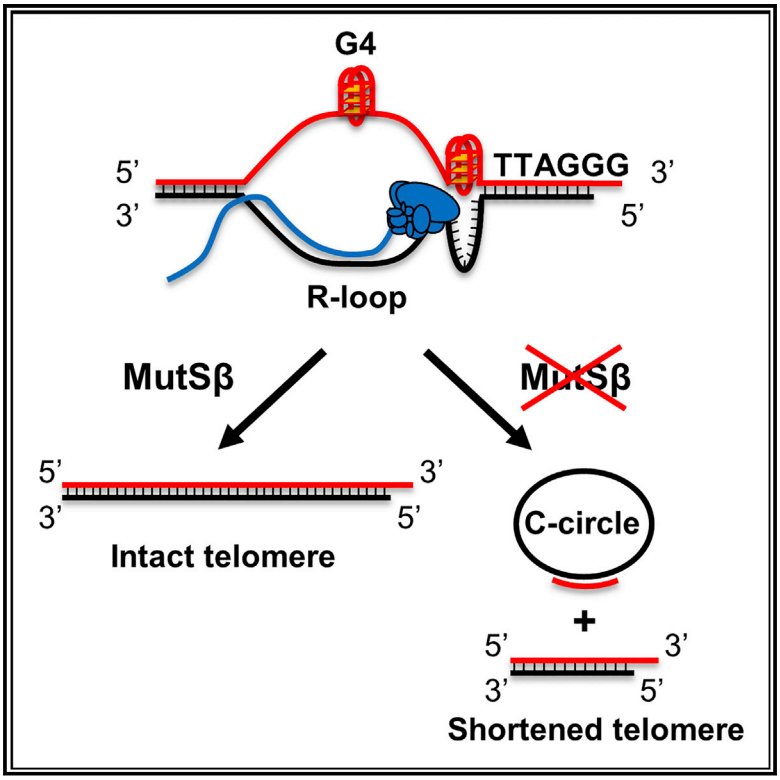

Highlights

- MSH2-MSH3 heterodimer (MutSβ) accumulates at telomeres in ALT cancer cells
- MutSβ protects ALT telomeres from fragility and loss
- MutSβ prevents accumulation of telomeric G4 structures and R-loops
- MutSβ binds to and destabilizes G4 structures *in vitro*

Authors

Despoina Sakellariou, Sara Thornby Bak, Esin Isik, ..., Jiri Bartek, Pavel Janscak, Javier Peña-Diaz

Correspondence

pjanscak@imcr.uzh.ch (P.J.), jdiaz@sund.ku.dk (J.P.-D.)

In brief

This study describes a function for the mismatch repair factor MutSβ in maintaining telomere integrity in ALT cancer cells. Sakellariou et al. show that MutSβ regulates accumulation of telomeric G-quadruplex structures and R-loops to prevent telomere trimming and formation of C-circles.

Sakellariou et al., 2022, Cell Reports *39*, 110602
April 5, 2022
https://doi.org/10.1016/j.celrep.2022.110602

CellPress

Cell Reports

CellPress
OPEN ACCESS

Article

MutSβ regulates G4-associated telomeric R-loops to maintain telomere integrity in ALT cancer cells

Despoina Sakellariou,[1,2] Sara Thornby Bak,[1,7] Esin Isik,[3,7] Sonia I. Barroso,[4] Antonio Porro,[3] Andrés Aguilera,[4] Jiri Bartek,[2,5,6] Pavel Janscak,[3,6,*] and Javier Peña-Diaz[1,8,*]

[1]Center for Healthy Aging, Department of Neuroscience and Pharmacology, University of Copenhagen, 2200 Copenhagen, Denmark
[2]Danish Cancer Society Research Center, 2100 Copenhagen, Denmark
[3]Institute of Molecular Cancer Research, University of Zurich, 8057 Zürich, Switzerland
[4]Centro Andaluz de Biología Molecular y Medicina Regenerativa CABIMER, University of Seville-CSIC-UPO, Seville, Spain
[5]Division of Genome Biology, Department of Medical Biochemistry and Biophysics, Science for Life Laboratory, Karolinska Institute, 17177 Stockholm, Sweden
[6]Institute of Molecular Genetics, Academy of Sciences of the Czech Republic, 14300 Prague, Czech Republic
[7]These authors contributed equally
[8]Lead contact
*Correspondence: pjanscak@imcr.uzh.ch (P.J.), jdiaz@sund.ku.dk (J.P.-D.)
https://doi.org/10.1016/j.celrep.2022.110602

SUMMARY

Up to 15% of human cancers maintain their telomeres through a telomerase-independent mechanism, termed "alternative lengthening of telomeres" (ALT) that relies on homologous recombination between telomeric sequences. Emerging evidence suggests that the recombinogenic nature of ALT telomeres results from the formation of RNA:DNA hybrids (R-loops) between telomeric DNA and the long-noncoding telomeric repeat-containing RNA (TERRA). Here, we show that the mismatch repair protein MutSβ, a heterodimer of MSH2 and MSH3 subunits, is enriched at telomeres in ALT cancer cells, where it prevents the accumulation of telomeric G-quadruplex (G4) structures and R-loops. Cells depleted of MSH3 display increased incidence of R-loop-dependent telomere fragility and accumulation of telomeric C-circles. We also demonstrate that purified MutSβ recognizes and destabilizes G4 structures *in vitro*. These data suggest that MutSβ destabilizes G4 structures in ALT telomeres to regulate TERRA R-loops, which is a prerequisite for maintenance of telomere integrity during ALT.

INTRODUCTION

Unlimited cell proliferation requires a mechanism counteracting telomere attrition, which otherwise occurs in each cell cycle (Harley et al., 1990; Shay and Wright, 2019). In most human cancers, this is achieved through upregulation of telomerase activity, but 10%–15% of cancers possess a mechanism known as alternative lengthening of telomeres (ALT) that relies on homologous recombination (HR) between telomeric sequences (Reddel, 2003). The tumor types where ALT is prevalent include glioblastoma multiforme (the most common type of primary malignant brain tumor in adults), osteosarcomas, and soft tissue sarcomas, and patients with these tumors tend to have a particularly poor prognosis (Dilley and Greenberg, 2015). Contrary to the telomerase$^+$ cancers where telomerase-inhibition-based therapies hold promise, the search for ALT-specific therapeutic targets has yet to yield viable candidates. The hallmarks of ALT include (1) a unique pattern of telomere length heterogeneity; (2) rapid changes in individual telomere lengths; (3) an elevated frequency of exchange between telomeres; (4) elevated levels of the long noncoding telomeric repeat-containing RNA (TERRA); (5) an abundance of extrachromosomal circular telomeric DNA (T-circles), in particular of T-circles that contain a nick or gap in the G-rich strand (C-circles); and (6) the presence of ALT-associated promyelocytic leukemia bodies (APBs) (Cesare and Reddel, 2010). APBs contain telomeric DNA and proteins involved in telomere binding (TRF1 and TRF2), DNA replication, repair, and recombination (RPA, BLM, WRN, RAD51, RAD52, and MRE11/RAD50/NBS1; Henson et al., 2002).

Recent studies have suggested that the recombinogenic potential of telomeres in ALT cells results from TERRA transcription and subsequent formation of RNA:DNA hybrids (R-loops) between the TERRA transcript and the C-rich telomeric strand, which could facilitate invasion of the 3′-overhang of independent chromosome ends to prime synthesis of new telomeric material (Arora et al., 2014; Silva et al., 2021; Yang et al., 2021). However, these TERRA-telomeric DNA hybrids are finely regulated by the RNA endonuclease RNaseH1 to maintain telomere integrity (Arora et al., 2014). Another control mechanism is provided by the FANCM-FAAP24 complex (Pan et al., 2019; Silva et al., 2019),

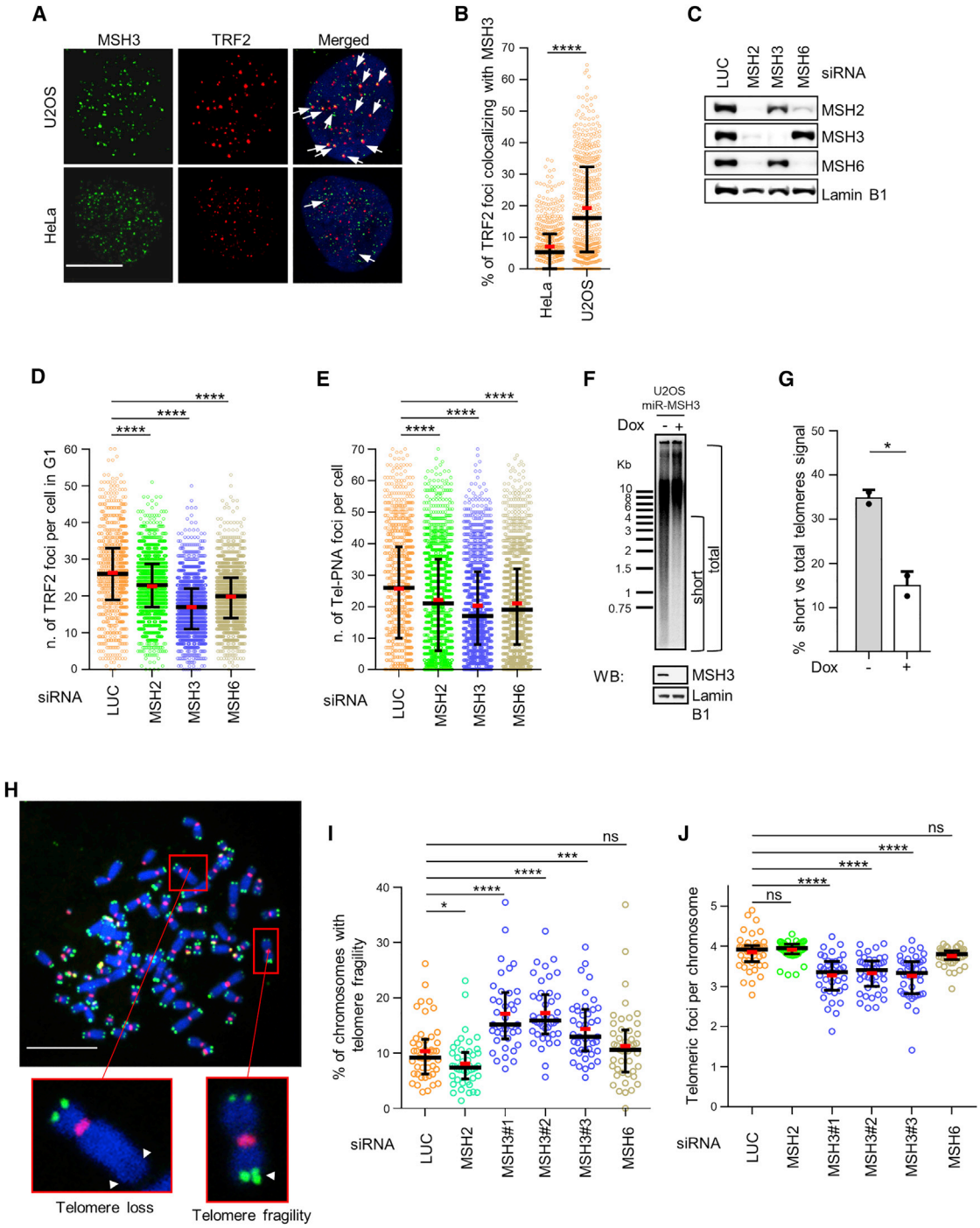

Figure 1. MutSβ accumulates at telomeres and maintains telomere integrity in ALT cancer cells

(A) Representative immunofluorescence images of MSH3 (green) and TRF2 (red) foci in nuclei (DAPI, blue) of U2OS and HeLa cells. Colocalizing foci are indicated by white arrows. Scale bar, 10 μm.

(B) Quantification of the percentage of TRF2 foci that colocalize with MSH3 foci in U2OS and HeLa cells. Median with interquartile range (black lines) and mean (red lines) are indicated. At least 516 nuclei from three independent experiments were analyzed for each condition.

(C) Immunoblot showing knockdown efficiency of indicated proteins in U2OS cells.

(D and E) Quantification of TRF2 foci (D) and telomere-PNA foci (E) in U2OS cells depleted for MSH2, MSH3, and MSH6, respectively. Median with interquartile range (black lines) and mean (red lines) are shown. At least 4,500 nuclei from three independent experiments were analyzed for each condition.

(legend continued on next page)

which can disrupt R-loops through its DNA translocase activity (Schwab et al., 2015; Silva et al., 2019). Loss of this activity increases R-loop-dependent replicative stress at telomeres and accumulation of telomeric C-circles in ALT cells (Pan et al., 2019; Silva et al., 2019). These findings highlight the relevance of regulatory mechanisms controlling R-loop abundance in the activation of recombination at ALT telomeres.

In yeast, defects in the mismatch repair (MMR) system have been shown to enhance telomerase-independent survival, with the survivors using recombination-based pathways for telomere maintenance (Rizki and Lundblad, 2001), suggesting a role for the MMR system as suppressor of telomeric recombination and ALT. However, the role of these proteins in telomere metabolism in ALT cancer cells remains to be explored. The canonical MMR is initiated by one of the two heterodimers: MSH2/MSH6 (MutSα) and MSH2/MSH3 (MutSβ). MutSα binds to base-base mismatches or insertion and deletion loops of 1–3 nt, while MutSβ binds to insertion and deletion loops containing up to 16 nt (Kunkel and Erie, 2015). MSH3 and MSH6 compete for binding to MSH2, and the heterodimer formation is required for their stability (Acharya et al., 1996). A recent study has shown that MutSα restricts telomere extension by ALT-associated homology-directed repair in human cancer cells (Barroso-Gonzalez et al., 2021). However, whether MutSβ plays a role in telomere metabolism in ALT cells remains to be explored.

Here, we identify MutSβ as a factor involved in the regulation of telomeric R-loops in ALT cancer cells, possibly by destabilizing G4 structures in the telomeric G-strand that promote R-loop formation and stability. Importantly, we show that lack of MutSβ increases the incidence of R-loop-dependent telomere fragility and the formation of telomeric C-circles in ALT cancer cells, providing further evidence that loss of regulation of TERRA R-loops can compromise telomere integrity.

RESULTS

MutSβ accumulates at telomeres and suppresses telomere fragility and loss in ALT cancer cells

Using proteomic approaches, the human MMR proteins MSH2, MSH6, MLH1, and PMS2 were found to be enriched at telomeres in ALT cells as compared with telomerase$^+$ cells (Garcia-Exposito et al., 2016). We could confirm these findings by immunofluorescence analyses showing extensive colocalization of MSH2 and MSH6 foci with TRF2 foci in U2OS cells (ALT$^+$), but not in HeLa long telomere (LT) cells (telomerase$^+$; Figures S1A, S1B, and S1D). Moreover, in U2OS cells, we observed a significantly higher percentage of telomeres containing MSH3 foci as compared with both HeLa and HeLa LT cells (Figures 1A, 1B, and S1C–S1E), indicating that MSH3, analogously to MSH2 and MSH6, is enriched at telomeres in ALT cells. To explore the role of the MMR proteins in telomere metabolism, we first examined the effect of their depletion on the number of TRF2 foci in nuclei of U2OS cells. We observed that depletion of either of these proteins decreased the number of TRF2 foci in cells with a DNA content corresponding to G1 phase of the cell cycle, with the decrease in TRF2 foci being markedly larger in cells depleted of MSH3 (over 1.5-fold decrease) than in cells depleted of MSH2 or MSH6 (Figures 1C and 1D). Similar results were obtained using three different small interfering RNAs (siRNAs) against MSH3 mRNA, excluding an siRNA off-target effect (Figures S2A and S2B). In HeLa LT cells, depletion of MSH2 or MSH6 did not significantly affect the number of TRF2 foci, and depletion of MSH3 resulted only in a marginal decrease of TRF2 foci (1.1-fold decrease; Figure S2C). To exclude the possibility that depletion of MMR proteins in U2OS cells impaired TRF2 loading on telomeres, we visualized telomeric DNA by fluorescence *in situ* hybridization (FISH). We observed that the decrease in the number of TRF2 foci after depletion of MSH2, MSH6, or MSH3 correlated with a decrease in the number of telomeric foci (over 1.5-fold decrease in MSH3-depleted cells; Figures 1E and S2D), suggesting that it is caused by loss of telomeric DNA. Telomeres in ALT cells display long-range movement and form multi-telomeric clusters where recombination takes place (Cho et al., 2014). Given that the MMR system controls recombination events by rejecting recombination between non-identical sequences (Goldfarb and Alani, 2005) and that subtelomeric regions contain dispersed telomeric repeats that may serve as imperfect HR templates (Linardopoulou et al., 2005), the loss of telomeric foci after depletion of MMR proteins could be due to an increase in telomeric clustering and recombination events. However, depletion of the MMR proteins did not lead to significant changes in intensity or size of telomere signals that could arise from either telomere clustering or end-to-end fusions (Figures S2E and S2F). Thus, our data rather suggest that depletion of the MMR proteins, particularly MSH3 depletion, leads to loss of telomeric DNA in U2OS cells.

The decrease in telomeric foci detected by immunofluorescence and the absence of changes in intensity or size of telomeric signals suggest that a subset of telomeres in MSH3-depleted cells become shorter and fall under the detection limit.

(F) Upper panel: TRF analysis of telomere length upon long-term depletion of MSH3. Autoradiography obtained after Southern blot and hybridization with a telomere probe is shown. Indicated regions were used for comparing intensities obtained from short telomeres (<4 kb) and total intensities (loading control). Lower panel: representative immunoblot shows doxycycline-dependent depletion of MSH3 after 30 days.

(G) Bar plot showing mean ± SD of percentage of short versus total telomere signal obtained from two independent experiments. Statistical analyses were performed using Student's t test. *$p < 0.05$.

(H) FISH analysis of a metaphase spread of MSH3-depleted U2OS cells showing centromeric (red) and telomeric DNA (green). In red boxes, examples of chromosomes exhibiting telomere fragility (bottom panel) and loss (top panel) are shown. The white arrowheads indicate fragile telomere and telomere loss, respectively. Scale bar, 10 μm.

(I) Scatterplot showing the percentage of metaphase chromosomes that exhibit telomere fragility for U2OS cells depleted of indicated proteins.

(J) Quantification of telomeric foci per metaphase chromosome for U2OS cells depleted of indicated proteins.

(I and J) At least 38 metaphases from three independent experiments were scored for each condition. Median with interquartile range (black lines) and mean (red lines) are indicated. ns, not significant; *$p < 0.05$, ***$p < 0.001$, and ****$p < 0.0001$ (Mann-Whitney test). (B, D, and E) ****$p < 0.0001$ (Mann-Whitney test). See also Figures S1–S4.

To address this, we examined the alterations in telomere length after long-term depletion of MSH3 in U2OS cells. We generated an inducible system using miR-RNAi that targets MSH3 mRNA with sustainable effects after addition of doxycycline (Dox). Selected clones were cultured for 30 days in the presence or absence of Dox (Figure S2G), and telomere length was then analyzed using the terminal restriction fragment (TRF) assay. We observed that MSH3 depletion caused loss of telomeric signals corresponding to short telomeres (Figures 1F, 1G, S2H, and S2I), while MSH2 or MSH6 depletion had no detectable effect on telomere length under our experimental settings. These results correlate with the observed reduction in telomeric foci in MSH3-depleted cells and suggest that short telomeres may be particularly vulnerable to attrition upon MSH3 depletion in U2OS cells.

The decrease in telomere length may lead to dysfunctional telomeres, which can elicit the DNA damage response (Takai et al., 2003). Thus, we analyzed the effect of depletion of MMR proteins on the level of the DNA-damage markers 53BP1 and γH2AX at telomeres in U2OS cells (telomere dysfunction-induced foci [TIFs]). We observed that depletion of MSH3 increased the number of TIFs in U2OS cells (Figures S3A–S3D). On the contrary, depletion of MSH2 rather reduced TIF frequency as compared with control and MSH6 depletion had no apparent effect (Figures S3A–S3D). Because MSH2 is present in both MutSβ and MutSα, these results suggest opposite effects of MutSβ and MutSα on telomere integrity. DNA-damage response factors are known to colocalize with APBs, and dysfunctional telomeres are associated with promyelocytic leukaemia (PML) in ALT-positive cells (Chung et al., 2012). In this regard, we observed an elevated association of telomeres with PML bodies upon depletion of MSH3 in U2OS cells (1.7-fold increase; Figures S3E and S3F), supporting the role of MutSβ in preventing telomere damage in ALT cells.

Next, we analyzed metaphase chromosome spreads by FISH and chromosome orientation FISH (CO-FISH) techniques to identify the alterations at telomeres in U2OS cells depleted of MMR proteins. Our results showed that MSH3 depletion significantly increased telomere fragility in the ALT cell lines U2OS, VA-13, and Saos2 (1.4-, 1.8-, and 1.7-fold increase, respectively; Figures 1H, 1I, and S4A), but not in the telomerase$^+$ HeLa LT cells. On the contrary, MSH2, but not MSH6, depletion rather decreased telomere fragility in U2OS cells (Figure 1I), suggesting a role for the MutSα heterodimer in promoting telomere fragility in absence of MSH3. Telomeric fragmentation in absence of MSH3 was not accompanied by significant or consistent changes in the levels of telomeric sister chromatid exchanges (T-SCEs) (Figures S4C–S4E) or interstitial telomeric repeats (ITRs) (Figures S4H–S4J). Importantly, we observed that MSH3 depletion increased the frequency of telomere loss in the ALT cancer cell lines U2OS and Saos2, but not in ALT-positive SV40 large T-antigen-transformed VA-13 fibroblasts and the telomerase$^+$ HeLa LT cells (Figures 1H, 1J, and S4B). In addition, we observed that MSH3 depletion caused loss of the G-rich telomere lagging strand in U2OS cells (Figures S4C, S4D, S4F, and S4G). Thus, we conclude that MutSβ suppresses telomere loss in ALT cancer cells.

MutSβ depletion causes accumulation of circular extrachromosomal telomeric DNA in ALT cancer cells

Inappropriate processing of telomere ends may result in fragility and/or loss of telomeric sequence as circular extrachromosomal telomeric DNA (Vannier et al., 2012). Thus, we investigated whether the telomere loss observed after depletion of MSH3 in U2OS cells is associated with an increase in the formation of telomeric circles. Given that MMR proteins are enriched at telomeres in ALT cancer cells, we focused on analyzing formation of ALT-specific C-circles using the rolling circle amplification assay (Henson et al., 2009; Figure S5A). We found that depletion of MSH3 increased the levels of telomeric C-circles in U2OS cells (Figures 2A, 2B, S5B, and S5C). On the contrary, MSH2 depletion decreased C-circle levels compared with control and depletion of MSH6 reduced C-circle levels in MSH3-depleted cells (Figures 2A and 2B). These results suggest the possibility of opposing roles for MutSβ and MutSα in modulating C-circle formation. In support of this notion, depletion of MSH3 did not increase C-circles levels in MSH2-knockout U2OS cells (Figures 2C and 2D).

To determine whether the increased formation of C-circles observed upon MSH3 depletion is specific to ALT cancer cells, we compared C-circle levels in various ALT (U2OS, Saos2, and VA-13) and telomerase$^+$ (A172, HeLa, and HEK293) cell lines. This analysis revealed that MSH3 depletion increased C-circle levels in the ALT cancer cell lines, U2OS and Saos2, but not in the immortalized ALT-positive VA-13 fibroblasts (Figures 2E and 2F), which exhibit relatively low levels of TERRA transcription (Arora et al., 2014; Toubiana et al., 2021). Importantly, depletion of MSH3 did not induce C-circle formation in any of the telomerase$^+$ cell lines tested (Figures 2E and 2F).

The SLX4 nuclease complex associates with telomeres in both telomerase$^+$ and ALT$^+$ cells through direct binding to TRF2 and, in absence of RTEL1, inappropriately resolves t-loops, resulting in telomere loss as a circle (Sarkar et al., 2015; Vannier et al., 2012). Intriguingly, SLX4 also interacts with MutSβ (Svendsen et al., 2009). Therefore, we investigated whether SLX4-associated nucleases, namely MUS81 and XPF, are also involved in the formation of C-circles observed upon MSH3 depletion in U2OS cells. We found that depletion of MUS81 or XPF attenuated C-circle formation induced by MSH3 deficiency (Figures 2G and 2H).

Together, these results suggest that MutSβ prevents the endonucleolytic processing of telomeric DNA to C-circles in ALT cancer cells.

MutSβ suppresses accumulation of telomeric G4 structures

We next focused on identifying the causes of the telomere integrity breakdown in cells lacking MutSβ. We investigated whether C-circle formation in MSH3-deficient U2OS cells was caused by telomeric G4 DNA structures that have been shown to be a major source of telomere fragility (Vannier et al., 2012). To address this, we treated U2OS cells with the G4-stabilizing ligand pyridostatin (PDS) and visualized the sites of G4 formation by immunofluorescence staining with BG4 antibody that specifically binds to G4 structures. We observed an increase in the number of nuclear BG4 foci after depletion of MSH3

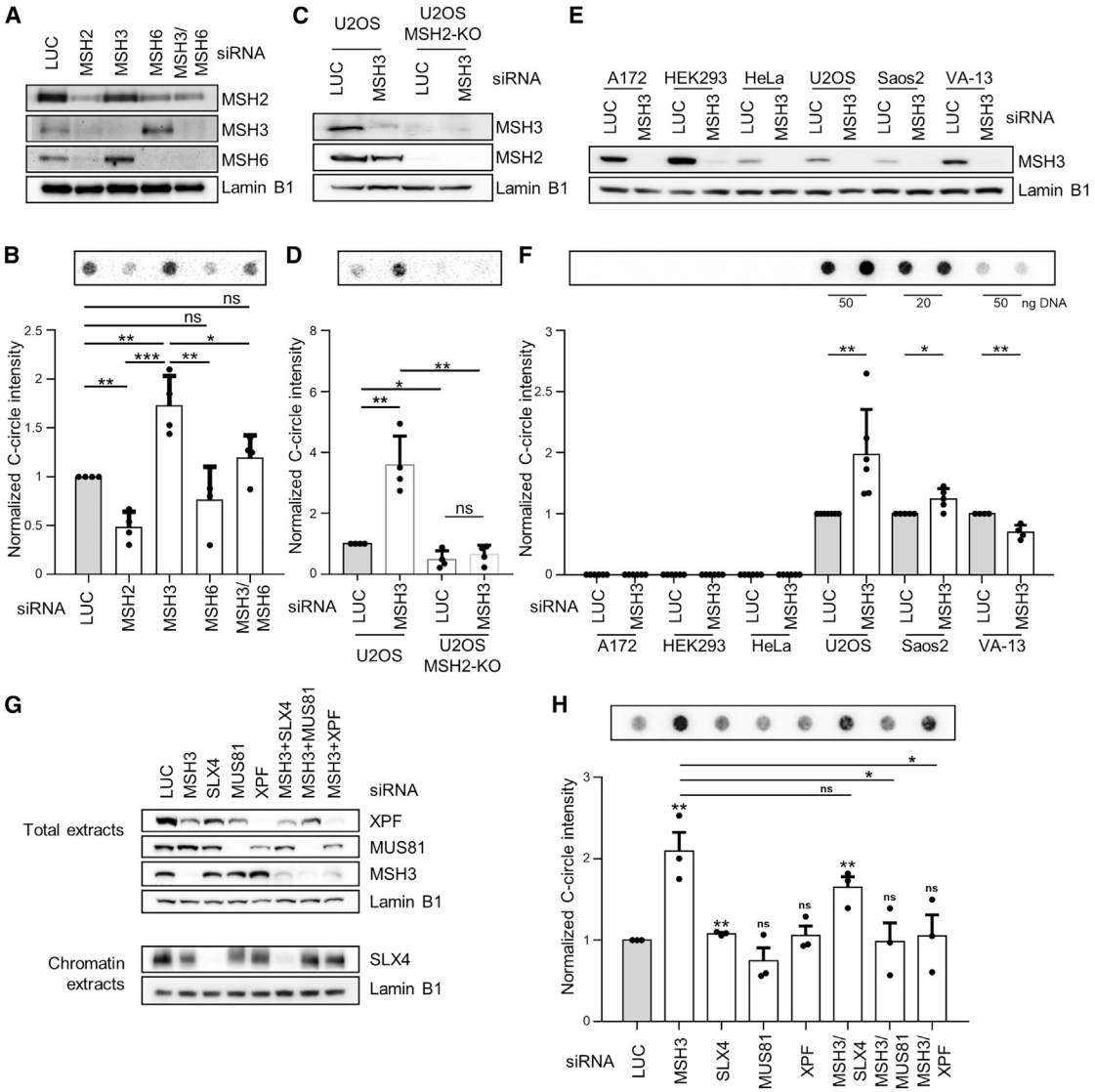

Figure 2. MutSβ suppresses telomeric C-circle formation in ALT cancer cells

(A, C, and E) Representative immunoblots related to (B), (D), and (F), respectively.

(B, D, and F) Representative dot blot of Phi29-dependent C-circle assay products (upper panel) and quantitation of C-circle intensity (lower panel) for (B) U2OS cells depleted of the indicated MMR proteins, (D) U2OS and U2OS MSH2 knockout cells transfected with control (siLUC) or MSH3 (siMSH3) siRNA, and (F) the telomerase$^+$ cell lines A172, HEK293, and HeLa and the ALT cell lines U2OS, Saos2, and VA-13 transfected with siLUC or siMSH3 (the amount of DNA [ng] used for Phi29-dependent C-circle amplification is indicated below the dot blot). C-circle intensity values are normalized to siLUC. Data represent the mean ± SD (n = 3). *p < 0.05, **p < 0.01, and ***p < 0.001 (two-tailed unpaired t test).

(G) Representative immunoblots showing knockdown efficiency of the indicated proteins in U2OS cells. Chromatin extracts were used for SLX4 detection.

(H) Representative dot blots (top panel) and quantitation of C-circle intensity (bottom panel) for U2OS cells depleted of indicated proteins. C-circle intensity values are normalized to siLUC. Data are represented as mean ± SD (n = 3). *p < 0.05 and **p < 0.01 (two-tailed unpaired t test). p values above the bars refer to comparisons with siLUC.

See also Figure S5.

(1.2-fold increase; Figures 3A and S6A). Importantly, PDS treatment and MSH3 depletion synergistically increased the percentage of telomeres (TRF2 foci) colocalizing with G4 signal (Figure 3B), as well as the generation of C-circles (Figure 3C). The synergistic effect of PDS and MSH3 depletion on C-circle formation was not apparent at high doses of PDS (2 μM), likely due to saturation (Figure 3C). These results reveal an involvement of MutSβ in regulating the levels of G4 structures at telomeres, which may cause the formation of C-circles. Of note, MSH3 depletion also increased G4 levels at other genomic loci in U2OS cells (Figure S6B), suggesting a general role for MutSβ in regulating G4 levels.

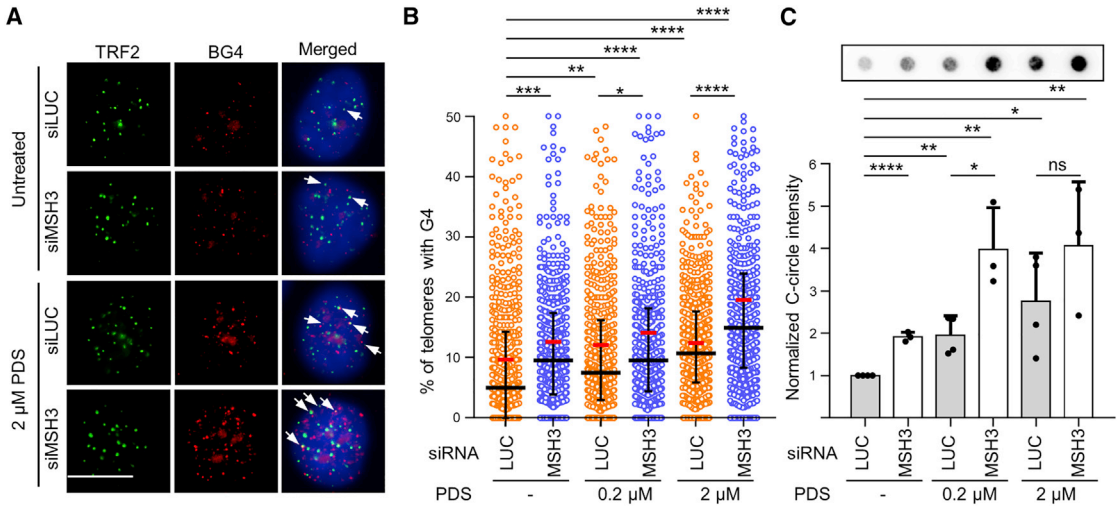

Figure 3. MutSβ suppresses accumulation of telomeric G4 structures in U2OS cells

(A) Representative immunofluorescence images of BG4 (red) and TRF2 (green) foci in U2OS cells transfected with siLUC or siMSH3 and either untreated or treated with 2 μM PDS for 1 h. Colocalizing foci are indicated with white arrows. Scale bar, 10 μm.

(B) Scatterplot showing the percentage of TRF2 foci colocalizing with BG4 foci in U2OS cells under specified conditions. PDS treatment was carried out for 1 h. At least 550 nuclei from three independent experiments were analyzed for each condition.

(C) Dot blot analysis of C-circle assay products (upper panel) and quantitation of C-circle intensity (lower panel) for U2OS cells (lower) after mock or MSH3 depletion and 3-h treatment with indicated concentrations of PDS.

Data represent the mean ± SD (n = 3). *p < 0.05, **p < 0.01, and ****p < 0.0001 (two-tailed unpaired t test). See also Figure S6.

MutSβ recognizes and destabilizes G4 structures

To explore the possibility that MutSβ is directly involved in the processing of G4 structures, we utilized an *in vitro* reporter assay that monitors G4 stability through blockage of DNA synthesis. In this assay, we used a fluorescently tagged primer and an oligonucleotide template containing a G4-forming sequence flanked by a polyT sequence followed by the sequence complementary to the primer at the 3′ end (Figure 4A). Oligonucleotides were annealed using conditions that are known to promote G4 formation (a KCl-based buffer) and conditions that do not enhance G4 formation (buffers without salts or with NaCl). As expected, primer extension by Klenow fragment of *E. coli* DNA polymerase I was efficiently blocked at the G4-forming sequence if the oligos were annealed in KCl-based buffer, while a full primer extension was seen with oligos annealed in the absence of salts or in the presence of NaCl (Figure 4B). We first tested whether MutSβ was capable of recognizing such G4 structure by using purified recombinant MutSβ (Figure 4C) and fluorescently labeled oligonucleotide containing only the G4-forming sequence (Figure 4A), which was, following heat denaturation, incubated in buffer containing either no salt (unstructured G4 sequence) or KCl (G4 structure). We monitored MutSβ binding to each substrate by electrophoretic mobility shift assays and detected MutSβ bound to both substrates. However, addition of an unlabeled poly dT competitor resulted in a significant decrease in MutSβ binding to the non-structured substrate, while MutSβ binding to the G4 structure largely persisted upon poly dT addition (Figures 4D and 4E). These data show that MutSβ binds preferentially to G4 structures. MutSβ binding to structures such as insertion-deletion loops has been shown to severely bend the DNA and facilitate unpairing of a normal downstream base pair (Gupta et al., 2011). Thus, we sought to test whether MutSβ binding to G4 and its DNA-bending activity is capable of destabilizing the G4 block to DNA synthesis in the above reporter assay (Figure 4B). To this end, we preincubated the G4 substrate with MutSβ to allow its binding followed by a DNA synthesis step with Klenow. We observed that MutSβ alleviated the G4-dependent block to DNA synthesis, allowing incorporation of two nucleotides past the blockage site, and increased synthesis of the full-length primer extension product (Figures 4F and 4G). Together, these findings suggest that MutSβ possesses the ability to bind and destabilize G4 structures.

MutSβ prevents accumulation of R-loops at ALT telomeres

G4 structures formed during transcription or replication might cause transient stalling of the RNA polymerase II (RNA Pol II) complex (Scheibye-Knudsen et al., 2016) that may favor the formation of R-loops or, when formed in the exposed non-template G-rich strand, stabilize such structures and promote their extension (Aguilera and Garcia-Muse, 2012; De Magis et al., 2019). Accordingly, by DNA:RNA hybrid immunoprecipitation (DRIP) with S9.6 antibody followed by quantitative real-time PCR, we found that PDS treatment increased the level of telomeric R-loops in U2OS, but not in HeLa cells (Figure S7A). Moreover, PDS had no effect on R-loop accumulation in an R-loop-prone region of the *RPL13A* gene, which does not contain a G4-forming sequence (Figure S7A; Barroso et al., 2019). These data support the notion that G4s and G4-mediated R-loops are more frequently formed in ALT telomeres that undergo TERRA transcription than in telomeres in telomerase^{+} cells.

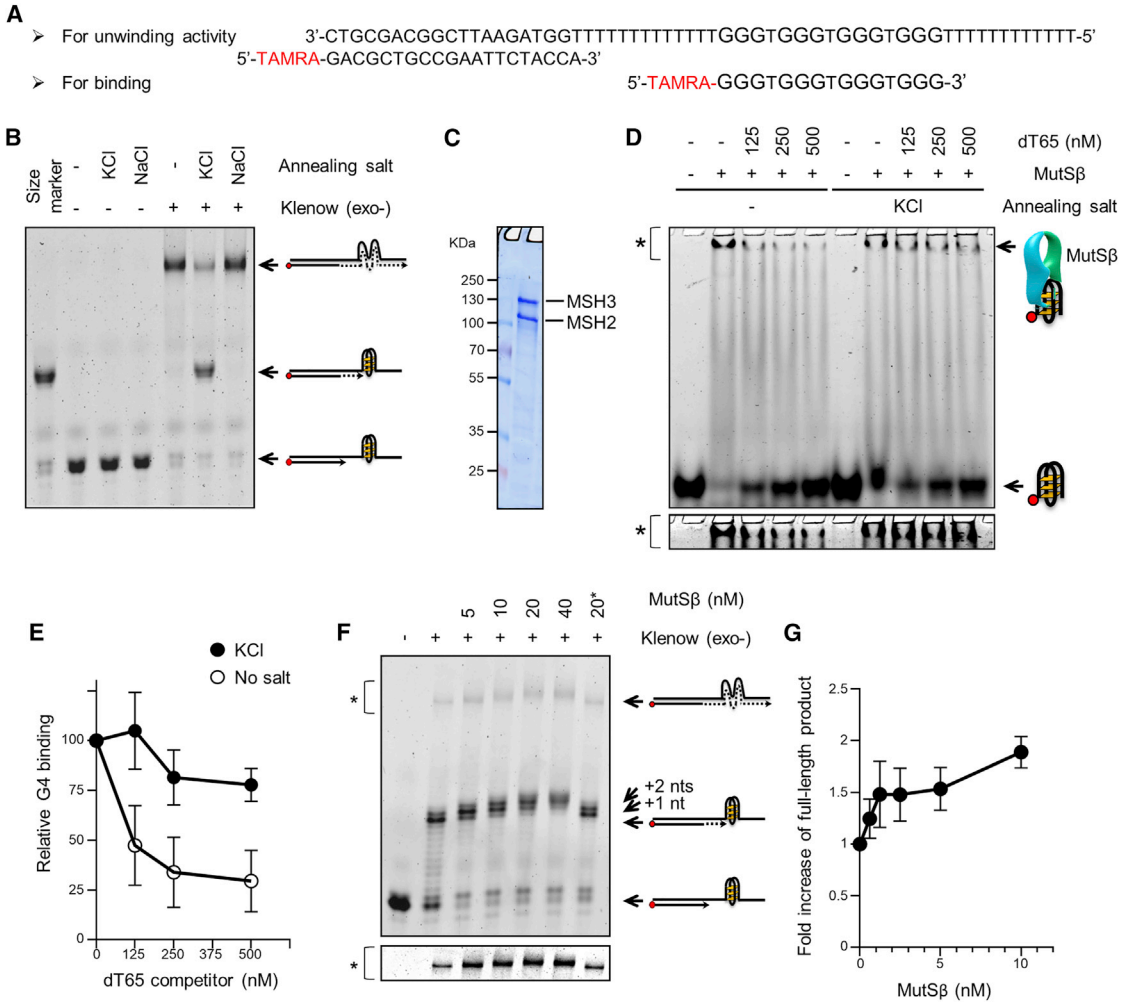

Figure 4. MutSβ recognizes and destabilizes G4 structures

(A) Oligonucleotides used for preparation of G4 substrates.

(B) Denaturing PAGE analysis showing the products of the Klenow primer extension reaction on the substrate in (A) annealed in buffers containing or not the indicated salts and deoxyribonucleotide triphosphates (dNTPs). The size marker was obtained by using the substrate prepared in NaCl-based buffer and performing the Klenow extension with dATP only. The schemes shown at the right depict the products of the reaction before denaturation.

(C) Coomassie-blue-stained SDS-PAGE gel showing purified recombinant MutSβ.

(D) Native PAGE analysis of MutSβ binding to substrates annealed in absence or in presence of KCl. dT65 oligo was used as competitor. The bands corresponding to the substrate bound to MutSβ (*) are shown enhanced for visualization purposes (lower panel). The schemes at the right depict the substrate alone and bound to MutSβ.

(E) Quantification of MutSβ binding to the substrates used in (D). Binding efficiency was normalized using the band intensities obtained with substrates incubated with MutSβ in absence of competitor. Data represent the mean ± SEM (n = 3).

(F) Denaturing PAGE analysis showing the products of Klenow primer extension reaction on the substrate annealed in KCl-based buffer that was preincubated with different concentrations of MutSβ prior to the extension. The last lane contains the products of reaction with heat-inactivated MutSβ (20*). The schemes shown at the right depict the products of the reaction before denaturation and include annotations for the bands that are 1 to 2 nt longer than the ones expected when extension is blocked at the first G of the quadruplex. The bands corresponding to full-length extension of the substrate (*) are shown enhanced for visualization purposes (lower panel).

(G) Normalized fold increase in full-length extension products obtained after addition of the indicated concentrations of MutSβ. Data represent the mean ± SEM (n = 3).

TERRA-telomeric hybrids have been shown to be the cause of C-circle formation in ALT cells (Arora et al., 2014). To explore a possible link between the elevated levels of C-circles observed after MSH3 depletion and the accumulation of G4/R-loops, we analyzed the effect of MSH3 depletion on R-loop levels in U2OS cells. By immunofluorescence staining using S9.6 antibody, we observed that depletion of MSH3, particularly in combination with PDS treatment, significantly increased the formation of R-loops in the cell nuclei, both at sites of telomeres and other nuclear loci (Figure 5A–5C). By DRIP-quantitative real-time

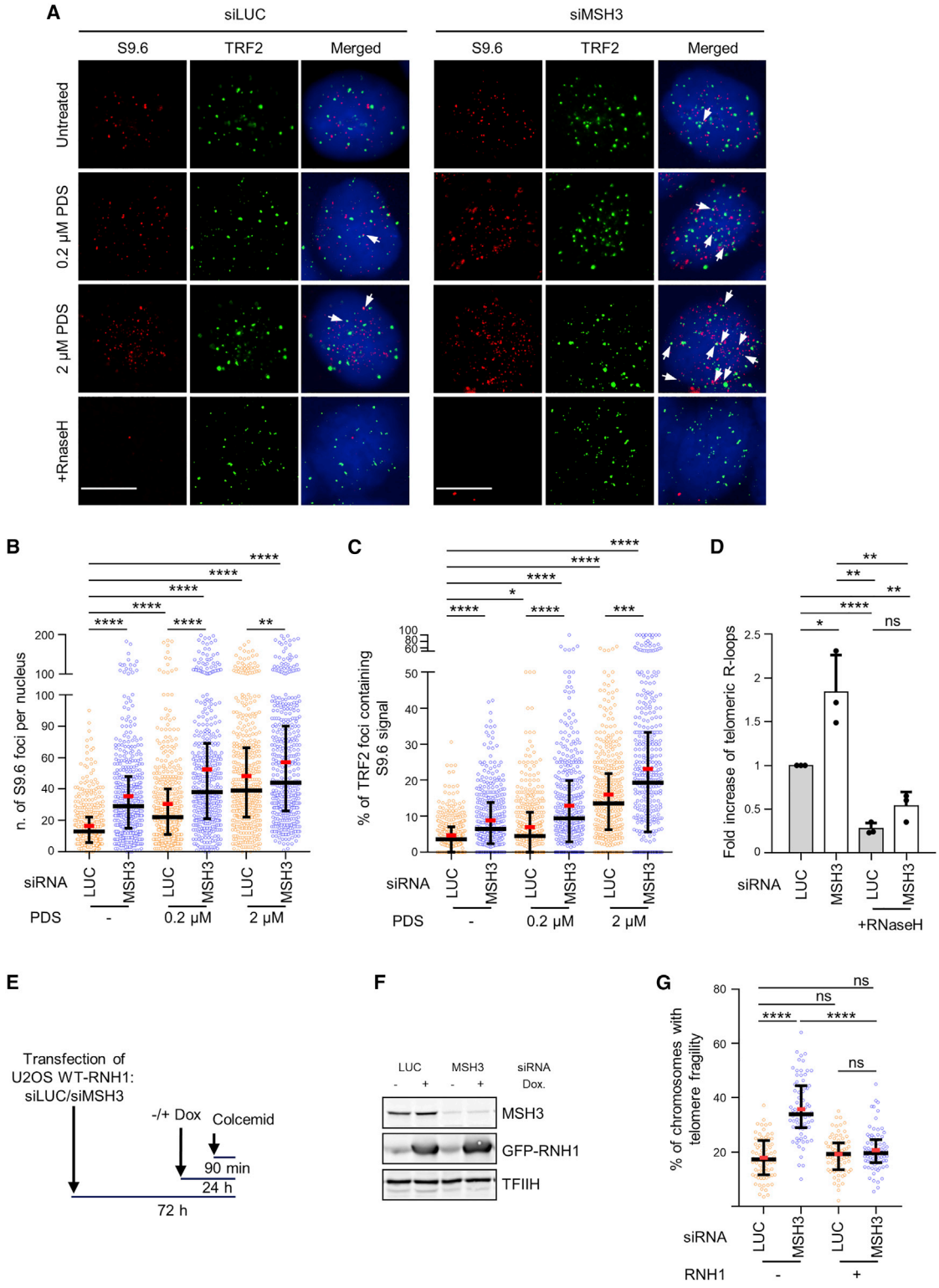

Figure 5. MutSβ prevents accumulation of R-loops at telomeres in U2OS cells

(A) Representative immunofluorescence images obtained using antibodies against RNA:DNA hybrids (S9.6, red) and TRF2 (green) after transfection of U2OS cells with control (siLUC) or MSH3 (siMSH3) siRNA and treatment with the indicated concentrations of pyridostatin (PDS) for 3 h. Treatment with RNaseH was used to exclude unspecific S9.6 signals. White arrows indicate colocalizing foci. Scale bars, 10 μm.

(legend continued on next page)

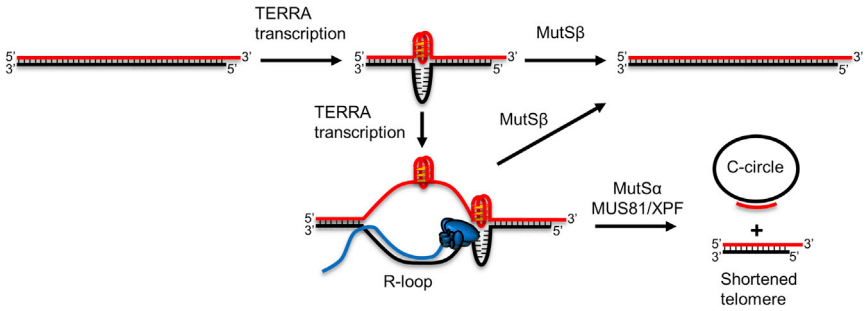

Figure 6. Model for the function of MutSβ at ALT telomeres

MutSβ, possibly in cooperation with DNA helicases, eliminates G4 structures to prevent formation of telomeric R-loops during TERRA transcription and/or to facilitate R-loop removal. In the absence of MutSβ, G4s promote R-loop formation by blocking RNA polymerase II and/or by stabilizing the R-loop structure. XPF and MUS81 endonucleases and MutSα process telomeric G4/R-loops and/or resulting DNA structures, leading to telomere fragility (not shown) and loss of telomeric DNA as a C-circle.

PCR, we could confirm that MSH3 depletion increased the level of telomeric R-loops in U2OS and Saos2 cells, but not in the telomerase$^+$ cells HeLa and A172 (Figures 5D and S7B). These results are consistent with the observed changes in C-circle levels after depletion of MSH3 in these cells (Figure 2F).

Recent work has provided evidence that TERRA R-loops trigger telomere fragility (Feretzaki et al., 2020). Therefore, we tested whether the increased telomere fragility observed after MSH3 depletion in U2OS cells (Figure 1I) is linked to the accumulation of R-loops. To address this point, we used a stable U2OS T-REx cell line carrying an RNaseH1 transgene under control of a doxycycline-regulatable cytomegalovirus (CMV) promoter (Chappidi et al., 2020). We found that ectopic overexpression of RNaseH1 suppressed telomere fragility induced by MSH3 depletion (Figures 5E–5G).

Collectively, these findings support a role for MutSβ in the regulation of G4-dependent telomeric R-loops in ALT cancer cells, which can give rise to telomere fragility and C-circle formation (Figure 6).

DISCUSSION

Loss of ATRX, a hallmark for ALT$^+$ cells, has been shown to cause TERRA upregulation and accumulation of G4 structures in telomeric DNA (Flynn et al., 2015; Wang et al., 2019). G4 structures pose a roadblock to the progression of DNA replication and transcription machineries, and failure to disassemble these structures results in telomere fragility (Ding et al., 2004; Sfeir et al., 2009; Vannier et al., 2012; Yang et al., 2021; Zimmer et al., 2016), a phenotype manifested by MSH3-deficient U2OS cells in this study (Figure 1I). We found that MutSβ suppresses accumulation of telomeric G4 structures in U2OS cells and can specifically bind and destabilize G4 structures *in vitro* (Figures 3, 4F, and 4G). These findings suggest a role for this heterodimer as a sensor of G4 structures and a factor involved in their dissolution. MutSβ may act in conjunction with a specific DNA helicase capable of G4 unwinding. Of note, two such helicases, namely FANCJ and WRN, localize to telomeres in ALT cells and interact directly with the MMR protein MLH1, which in the form of MLH1/PMS2 heterodimer binds to the complex of MutSα/β with mismatched DNA during the canonical MMR reaction (Guillemette et al., 2014; Kunkel and Erie, 2015; Peng et al., 2007; Saydam et al., 2007; Ward et al., 2012).

Unresolved G4s may promote the formation of telomeric structures that are processed endonucleolytically to C-circles. One such structure prevalent at ALT telomeres, because of the elevated levels of TERRA transcription, is R-loop (Arora et al., 2014; Silva et al., 2021). In this regard, telomeric G4s have recently been proposed as a novel hallmark of ALT cancers (Yang et al., 2021). Here, we show that MutSβ prevents accumulation of R-loops in telomeres of ALT cancer cells (Figures 5D and S7B). Moreover, our data suggest that the elevated telomere fragility observed in U2OS cells depleted of MutSβ depends on R-loops (Figure 5G). Although the formation of TERRA R-loops is essential for ALT, their excess can lead to excision of telomeric DNA in form of extrachromosomal C-circles (Arora et al., 2014). Evidence suggests that G4 structures stabilize R-loops and promote their extension (Aguilera and Garcia-Muse, 2012; De Magis et al., 2019). Thus, MutSβ could destabilize G4 structures formed in the G-rich strand during TERRA transcription and hence disfavor R-loop formation (Figure 6). Alternatively, by destabilizing G4 structures, MutSβ could facilitate R-loop removal (Figure 6), possibly by the FANCM-FAAP24 DNA translocase, which is known to regulate the levels of TERRA R-loops in ALT cells

(B) Quantification of S9.6 foci in nuclei of mock- and MSH3-depleted U2OS cells treated as in (A). Median with interquartile range (black lines) and mean (red lines) are indicated. *p < 0.05 and ****p < 0.0001 (Mann-Whitney test).
(C) Scatterplot showing the percentage of TRF2 foci colocalizing with S9.6 signal for cells in (A). At least 400 nuclei from three independent experiments were analyzed. **p < 0.01, ***p < 0.001, and ****p < 0.0001 (Mann-Whitney test).
(D) Quantitation of the level of telomeric R-loops in mock- and MSH3-depleted U2OS cells by DRIP-quantitative real-time PCR. Where indicated, genomic DNA was treated with RNaseH prior to immunoprecipitation with S9.6 antibody. Data are mean ± SD (n = 3) and are normalized to siLUC (no RNaseH). *p < 0.05, **p < 0.01, and ****p < 0.0001 (two-tailed unpaired t test).
(E) Scheme showing the steps followed to generate metaphase spreads from U2OS wild-type (WT)-RNH1 cells. Doxycycline (Dox) addition induces the overexpression of WT-RNH1. FISH with a C-rich telomere probe was used to examine telomere fragility.
(F) Representative immunoblot of total extracts from U2OS WT-RNH1 cells transfected with the indicated siRNAs and treated with Dox for 24 h or left untreated.
(G) Scatterplot showing percentage of metaphase chromosomes exhibiting telomeric fragility. Data correspond to 75 metaphases obtained from three independent experiments. Median with interquartile range (black lines) and mean (red lines) are indicated. ****p < 0.0001 (Mann-Whitney test).
See also Figure S7.

(Pan et al., 2019; Silva et al., 2019). It is possible that G4 structures within the G-rich telomeric strand impair the translocation of FANCM-FAAP24 along DNA, which drives the strand exchange reaction, leading to R-loop removal (Schwab et al., 2015).

We observed that absence of MutSβ increased telomeric C-circle levels in ALT cancer cells (Figures 2B and 2F). Although it is established that C-circle excision is promoted by TERRA R-loops (Arora et al., 2014) and TERRA transcription has recently been shown to initiate ALT by destabilizing telomere integrity (Silva et al., 2021), the underlying molecular mechanism and regulators of this process remain incompletely defined. It is possible that C-circles might form as a product of intratelomeric recombination facilitated by G4/R-loop structures. In support of this notion, we found that C-circle formation was stimulated by PDS treatment (Figure 3C), which also increased the level of telomeric RNA:DNA hybrids, particularly in MSH3-depleted U2OS cells (Figures 5C and S7A). In addition, we observed that accumulation of C-circles in MSH3-depleted U2OS cells is dependent on the structure-specific endonucleases MUS81 and XPF (Figure 2H). MUS81 endonuclease prefers substrates that contain a discontinuity or nick adjacent to the branchpoint of a junction (Schwartz and Heyer, 2011). XPF together with XPG have been previously shown to actively process R-loops into DNA double-strand breaks (Sollier et al., 2014). Interestingly, MUS81 and XPF are part of the SLX4-associated nuclease complex that is known to interact with telomeres through TRF2 binding (Svendsen et al., 2009). Thus, it is conceivable that cleavage of telomeric R-loops by these nucleases might create DNA intermediates involved in the formation of C-circles and/or DNA gaps detected as telomeric fragile sites (Figure 6).

Interestingly, we found that depletion of the MSH3 interaction partner, MSH2, lowered rather than increased telomere fragility and C-circle formation in U2OS cells (Figures 1I and 2D). Given that MSH3 and MSH6 compete for binding to MSH2, this suggests opposite roles for the heterodimers MutSα and MutSβ in telomere metabolism. Of note, MutSα is known to interact physically and functionally with the BLM helicase (Yang et al., 2004), which is required for C-circle formation in ALT cells (Lu et al., 2019; O'Sullivan et al., 2014; Zhang et al., 2019). Thus, in absence of MSH3, MutSα may interact with G4 and enhance recruitment and activity of BLM. Binding of MutSα to G4 has previously been demonstrated *in vitro* (Larson et al., 2005). Of note, we found that elevated levels of C-circles in MSH3-depleted U2OS cells depend not only on MutSα but also on BLM (Figure S5D).

Interestingly, we found that depletion of MSH3 increased G4 and R-loop formation also at non-telomeric sites in U2OS cells. Thus, MutSβ is likely to operate on G4s genome-wide. Further studies are needed to define the consequences of the failure of this activity of MutSβ.

In conclusion, here, we uncover a role for MutSβ in regulating G4 and R-loops in ALT telomeres to prevent telomere fragility and nucleolytic excision in form of C-circles. Whereas a lot of effort is placed in telomerase-inhibition-based therapies for cancer treatment, the incomplete knowledge on the molecular events governing ALT has hampered attempts to find targets for treatment of ALT-positive cancers. The need to find therapeutic interventions against ALT-cancer cells is stressed by the fact that several ALT cancers have a dismal prognosis. In addition, ALT cells may coexist with telomerase$^+$ cells in the same tumor and telomerase$^+$ cells may engage ALT mechanisms to escape telomerase inhibition. Our results constitute a step forward towards a better understanding of the ALT pathway that is needed for the development of additional therapeutic strategies exploiting ALT-associated vulnerabilities in ALT$^+$ tumors.

Limitations of the study

Our results represent a proof of principle showing the involvement of MutSβ in regulation of G4-associated telomeric R-loops to maintain telomere integrity in ALT cancer cells. Further studies are needed to establish the relative relevance of this mechanism in other ALT cell lines than those used in the current study.

STAR★METHODS

Detailed methods are provided in the online version of this paper and include the following:

- KEY RESOURCES TABLE
- RESOURCE AVAILABILITY
  - Lead contact
  - Materials availability
  - Data and code availability
- EXPERIMENTAL MODEL AND SUBJECT DETAILS
  - Cell lines and cell culture
- METHOD DETAILS
  - Small interference RNA transfections and treatment
  - Inducible knockdown of gene expression
  - Western blotting
  - Immunofluorescence assays
  - Fluorescent *in situ* hybridization (FISH)
  - Metaphase chromosome spreads
  - Chromosome orientation FISH (CO-FISH)
  - Rolling circle amplification assay
  - G-quadruplex biochemical assays
  - Terminal restriction fragment assay (TRF)
  - Detection of R-loops at telomeres by DNA:RNA hybrid immunoprecipitation (DRIP) followed by qPCR
- QUANTIFICATION AND STATISTICAL ANALYSIS

SUPPLEMENTAL INFORMATION

Supplemental information can be found online at https://doi.org/10.1016/j.celrep.2022.110602.

ACKNOWLEDGMENTS

We wish to thank Kai Neelsen, Stanislaw Jozwiakowski, Andres Lopez Contreras, and Ian Hickson for critical reading of the manuscript and helpful discussions. In addition, we would like to thank Diana Odermatt and Kerstin Gari for their advice with G4 assays. J.P.D. was supported by the Danish Council for Independent Research (DFF-4004-00117), the Danish Cancer Society (R72-A4181-13-S2), the Nordea Foundation, Agnes and Poul Friis Fond, and Magda Sofie and Aase Lutz Mindelegat. P.J. was supported by the Swiss National Science Foundation (310030_184716) and Czech Science Foundation (19-07674S). J.B. was supported by the Danish Council for Independent

Research (DFF-7016-00313), the Danish Cancer Society (R204-A12617), the Novo Nordisk Foundation (200C0060590), the Czech Science Foundation (project 19-21325S), the Swedish Research Council (VR-MH 2014-46602-117891-30), and the Swedish CancerFonden (no. 170176) and A.A. by the European Research Council (ERC2014 AdG669898 TARLOOP), the Spanish Ministry of Science and Innovation (PID2019-104270GB-I00/BMC), and the European Union (FEDER).

AUTHOR CONTRIBUTIONS

Conceptualization, D.S., P.J., and J.P.-D.; methodology, D.S., S.I.B., E.I., S.T.B., A.P., A.A., P.J., and J.P.-D.; investigation, D.S., S.I.B., E.I., S.T.B., A.P., A.A., P.J., and J.P.-D.; supervision, A.A., J.B., P.J., and J.P.-D.; writing – original draft, P.J. and J.P.-D.; writing – review & editing, D.S., S.T.B., E.I., S.I.B., A.P., A.A., J.B., P.J., and J.P.-D.

DECLARATION OF INTERESTS

The authors declare no competing interests.

Received: July 1, 2021
Revised: December 17, 2021
Accepted: March 10, 2022
Published: April 5, 2022

REFERENCES

Acharya, S., Wilson, T., Gradia, S., Kane, M.F., Guerrette, S., Marsischky, G.T., Kolodner, R., and Fishel, R. (1996). hMSH2 forms specific mispair-binding complexes with hMSH3 and hMSH6. Proc. Natl. Acad. Sci. U S A *93*, 13629–13634.

Aguilera, A., and Garcia-Muse, T. (2012). R loops: from transcription byproducts to threats to genome stability. Mol. Cell *46*, 115–124.

Arora, R., Lee, Y., Wischnewski, H., Brun, C.M., Schwarz, T., and Azzalin, C.M. (2014). RNaseH1 regulates TERRA-telomeric DNA hybrids and telomere maintenance in ALT tumour cells. Nat. Commun. *5*, 5220.

Barroso-Gonzalez, J., Garcia-Exposito, L., Galaviz, P., Lynskey, M.L., Allen, J.A.M., Hoang, S., Watkins, S.C., Pickett, H.A., and O'Sullivan, R.J. (2021). Anti-recombination function of MutSalpha restricts telomere extension by ALT-associated homology-directed repair. Cell Rep. *37*, 110088.

Barroso, S., Herrera-Moyano, E., Munoz, S., Garcia-Rubio, M., Gomez-Gonzalez, B., and Aguilera, A. (2019). The DNA damage response acts as a safeguard against harmful DNA-RNA hybrids of different origins. EMBO Rep. *20*, e47250.

Biffi, G., Tannahill, D., McCafferty, J., and Balasubramanian, S. (2013). Quantitative visualization of DNA G-quadruplex structures in human cells. Nat. Chem. *5*, 182–186.

Boque-Sastre, R., Soler, M., and Guil, S. (2017). Detection and characterization of R loop structures. Methods Mol. Biol. *1543*, 231–242.

Burdova, K., Mihaljevic, B., Sturzenegger, A., Chappidi, N., and Janscak, P. (2015). The mismatch-binding factor MutSbeta can mediate ATR activation in response to DNA double-strand breaks. Mol. Cell *59*, 603–614.

Cawthon, R.M. (2009). Telomere length measurement by a novel monochrome multiplex quantitative PCR method. Nucleic Acids Res. *37*, e21.

Cesare, A.J., and Reddel, R.R. (2010). Alternative lengthening of telomeres: models, mechanisms and implications. Nat. Rev. Genet. *11*, 319–330.

Chappidi, N., Nascakova, Z., Boleslavska, B., Zellweger, R., Isik, E., Andrs, M., Menon, S., Dobrovolna, J., Balbo Pogliano, C., Matos, J., et al. (2020). Fork cleavage-religation cycle and active transcription mediate replication restart after fork stalling at Co-transcriptional R-loops. Mol. Cell *77*, 528–541.e528.

Cho, N.W., Dilley, R.L., Lampson, M.A., and Greenberg, R.A. (2014). Interchromosomal homology searches drive directional ALT telomere movement and synapsis. Cell *159*, 108–121.

Chung, I., Osterwald, S., Deeg, K.I., and Rippe, K. (2012). PML body meets telomere: the beginning of an ALTernate ending? Nucleus *3*, 263–275.

De Magis, A., Manzo, S.G., Russo, M., Marinello, J., Morigi, R., Sordet, O., and Capranico, G. (2019). DNA damage and genome instability by G-quadruplex ligands are mediated by R loops in human cancer cells. Proc. Natl. Acad. Sci. U S A *116*, 816–825.

Dilley, R.L., and Greenberg, R.A. (2015). ALTernative telomere maintenance and cancer. Trends Cancer *1*, 145–156.

Ding, H., Schertzer, M., Wu, X., Gertsenstein, M., Selig, S., Kammori, M., Pourvali, R., Poon, S., Vulto, I., Chavez, E., et al. (2004). Regulation of murine telomere length by Rtel: an essential gene encoding a helicase-like protein. Cell *117*, 873–886.

Feretzaki, M., Pospisilova, M., Valador Fernandes, R., Lunardi, T., Krejci, L., and Lingner, J. (2020). RAD51-dependent recruitment of TERRA lncRNA to telomeres through R-loops. Nature *587*, 303–308.

Flynn, R.L., Cox, K.E., Jeitany, M., Wakimoto, H., Bryll, A.R., Ganem, N.J., Bersani, F., Pineda, J.R., Suva, M.L., Benes, C.H., et al. (2015). Alternative lengthening of telomeres renders cancer cells hypersensitive to ATR inhibitors. Science *347*, 273–277.

Garcia-Exposito, L., Bournique, E., Bergoglio, V., Bose, A., Barroso-Gonzalez, J., Zhang, S., Roncaioli, J.L., Lee, M., Wallace, C.T., Watkins, S.C., et al. (2016). Proteomic profiling reveals a specific role for translesion DNA polymerase eta in the alternative lengthening of telomeres. Cell Rep. *17*, 1858–1871.

Garcia-Rubio, M., Barroso, S.I., and Aguilera, A. (2018). Detection of DNA-RNA hybrids in vivo. Methods Mol. Biol. *1672*, 347–361.

Goldfarb, T., and Alani, E. (2005). Distinct roles for the Saccharomyces cerevisiae mismatch repair proteins in heteroduplex rejection, mismatch repair and nonhomologous tail removal. Genetics *169*, 563–574.

Guberman, J.M., Ai, J., Arnaiz, O., Baran, J., Blake, A., Baldock, R., Chelala, C., Croft, D., Cros, A., Cutts, R.J., et al. (2011). BioMart central portal: an open database network for the biological community. Database *2011*, bar041.

Guillemette, S., Branagan, A., Peng, M., Dhruva, A., Scharer, O.D., and Cantor, S.B. (2014). FANCJ localization by mismatch repair is vital to maintain genomic integrity after UV irradiation. Cancer Res. *74*, 932–944.

Gupta, S., Gellert, M., and Yang, W. (2011). Mechanism of mismatch recognition revealed by human MutSbeta bound to unpaired DNA loops. Nat. Struct. Mol. Biol. *19*, 72–78.

Harley, C.B., Futcher, A.B., and Greider, C.W. (1990). Telomeres shorten during ageing of human fibroblasts. Nature *345*, 458–460.

Henson, J.D., Cao, Y., Huschtscha, L.I., Chang, A.C., Au, A.Y., Pickett, H.A., and Reddel, R.R. (2009). DNA C-circles are specific and quantifiable markers of alternative-lengthening-of-telomeres activity. Nat. Biotechnol. *27*, 1181–1185.

Henson, J.D., Neumann, A.A., Yeager, T.R., and Reddel, R.R. (2002). Alternative lengthening of telomeres in mammalian cells. Oncogene *21*, 598–610.

Kimura, M., Stone, R.C., Hunt, S.C., Skurnick, J., Lu, X., Cao, X., Harley, C.B., and Aviv, A. (2010). Measurement of telomere length by the Southern blot analysis of terminal restriction fragment lengths. Nat. Protoc. *5*, 1596–1607.

Kunkel, T.A., and Erie, D.A. (2015). Eukaryotic mismatch repair in relation to DNA replication. Annu. Rev. Genet. *49*, 291–313.

Larson, E.D., Duquette, M.L., Cummings, W.J., Streiff, R.J., and Maizels, N. (2005). MutSalpha binds to and promotes synapsis of transcriptionally activated immunoglobulin switch regions. Curr. Biol. *15*, 470–474.

Linardopoulou, E.V., Williams, E.M., Fan, Y., Friedman, C., Young, J.M., and Trask, B.J. (2005). Human subtelomeres are hot spots of interchromosomal recombination and segmental duplication. Nature *437*, 94–100.

Lu, R., O'Rourke, J.J., Sobinoff, A.P., Allen, J.A.M., Nelson, C.B., Tomlinson, C.G., Lee, M., Reddel, R.R., Deans, A.J., and Pickett, H.A. (2019). The FANCM-BLM-TOP3A-RMI complex suppresses alternative lengthening of telomeres (ALT). Nat. Commun. *10*, 2252.

Naito, Y., Hino, K., Bono, H., and Ui-Tei, K. (2015). CRISPRdirect: software for designing CRISPR/Cas guide RNA with reduced off-target sites. Bioinformatics *31*, 1120–1123.

O'Sullivan, R.J., Arnoult, N., Lackner, D.H., Oganesian, L., Haggblom, C., Corpet, A., Almouzni, G., and Karlseder, J. (2014). Rapid induction of alternative lengthening of telomeres by depletion of the histone chaperone ASF1. Nat. Struct. Mol. Biol. *21*, 167–174.

Pan, X., Chen, Y., Biju, B., Ahmed, N., Kong, J., Goldenberg, M., Huang, J., Mohan, N., Klosek, S., Parsa, K., et al. (2019). FANCM suppresses DNA replication stress at ALT telomeres by disrupting TERRA R-loops. Sci. Rep. *9*, 19110.

Peng, M., Litman, R., Xie, J., Sharma, S., Brosh, R.M., Jr., and Cantor, S.B. (2007). The FANCJ/MutLalpha interaction is required for correction of the cross-link response in FA-J cells. EMBO J. *26*, 3238–3249.

Perrem, K., Colgin, L.M., Neumann, A.A., Yeager, T.R., and Reddel, R.R. (2001). Coexistence of alternative lengthening of telomeres and telomerase in hTERT-transfected GM847 cells. Mol. Cell Biol. *21*, 3862–3875.

Ran, F.A., Hsu, P.D., Wright, J., Agarwala, V., Scott, D.A., and Zhang, F. (2013). Genome engineering using the CRISPR-Cas9 system. Nat. Protoc. *8*, 2281–2308.

Reddel, R.R. (2003). Alternative lengthening of telomeres, telomerase, and cancer. Cancer Lett. *194*, 155–162.

Rizki, A., and Lundblad, V. (2001). Defects in mismatch repair promote telomerase-independent proliferation. Nature *411*, 713–716.

Sarkar, J., Wan, B., Yin, J., Vallabhaneni, H., Horvath, K., Kulikowicz, T., Bohr, V.A., Zhang, Y., Lei, M., and Liu, Y. (2015). SLX4 contributes to telomere preservation and regulated processing of telomeric joint molecule intermediates. Nucleic Acids Res. *43*, 5912–5923.

Saydam, N., Kanagaraj, R., Dietschy, T., Garcia, P.L., Pena-Diaz, J., Shevelev, I., Stagljar, I., and Janscak, P. (2007). Physical and functional interactions between Werner syndrome helicase and mismatch-repair initiation factors. Nucleic Acids Res. *35*, 5706–5716.

Scheibye-Knudsen, M., Tseng, A., Borch Jensen, M., Scheibye-Alsing, K., Fang, E.F., Iyama, T., Bharti, S.K., Marosi, K., Froetscher, L., Kassahun, H., et al. (2016). Cockayne syndrome group A and B proteins converge on transcription-linked resolution of non-B DNA. Proc. Natl. Acad. Sci. U S A *113*, 12502–12507.

Schwab, R.A., Nieminuszczy, J., Shah, F., Langton, J., Lopez Martinez, D., Liang, C.C., Cohn, M.A., Gibbons, R.J., Deans, A.J., and Niedzwiedz, W. (2015). The fanconi anemia pathway maintains genome stability by coordinating replication and transcription. Mol. Cell *60*, 351–361.

Schwartz, E.K., and Heyer, W.D. (2011). Processing of joint molecule intermediates by structure-selective endonucleases during homologous recombination in eukaryotes. Chromosoma *120*, 109–127.

Sfeir, A., Kosiyatrakul, S.T., Hockemeyer, D., MacRae, S.L., Karlseder, J., Schildkraut, C.L., and de Lange, T. (2009). Mammalian telomeres resemble fragile sites and require TRF1 for efficient replication. Cell *138*, 90–103.

Shay, J.W., and Wright, W.E. (2019). Telomeres and telomerase: three decades of progress. Nat. Rev. Genet. *20*, 299–309.

Silva, B., Arora, R., Bione, S., and Azzalin, C.M. (2021). TERRA transcription destabilizes telomere integrity to initiate break-induced replication in human ALT cells. Nat. Commun. *12*, 3760.

Silva, B., Pentz, R., Figueira, A.M., Arora, R., Lee, Y.W., Hodson, C., Wischnewski, H., Deans, A.J., and Azzalin, C.M. (2019). FANCM limits ALT activity by restricting telomeric replication stress induced by deregulated BLM and R-loops. Nat. Commun. *10*, 2253.

Sollier, J., Stork, C.T., Garcia-Rubio, M.L., Paulsen, R.D., Aguilera, A., and Cimprich, K.A. (2014). Transcription-coupled nucleotide excision repair factors promote R-loop-induced genome instability. Mol. Cell *56*, 777–785.

Svendsen, J.M., Smogorzewska, A., Sowa, M.E., O'Connell, B.C., Gygi, S.P., Elledge, S.J., and Harper, J.W. (2009). Mammalian BTBD12/SLX4 assembles a Holliday junction resolvase and is required for DNA repair. Cell *138*, 63–77.

Takai, H., Smogorzewska, A., and de Lange, T. (2003). DNA damage foci at dysfunctional telomeres. Curr. Biol. *13*, 1549–1556.

Teloni, F., Michelena, J., Lezaja, A., Kilic, S., Ambrosi, C., Menon, S., Dobrovolna, J., Imhof, R., Janscak, P., Baubec, T., et al. (2019). Efficient pre-mRNA cleavage prevents replication-stress-associated genome instability. Mol. Cell *73*, 670–683.e612.

Toledo, L.I., Altmeyer, M., Rask, M.B., Lukas, C., Larsen, D.H., Povlsen, L.K., Bekker-Jensen, S., Mailand, N., Bartek, J., and Lukas, J. (2013). ATR prohibits replication catastrophe by preventing global exhaustion of RPA. Cell *155*, 1088–1103.

Toubiana, S., Tzur-Gilat, A., and Selig, S. (2021). Epigenetic characteristics of human subtelomeres vary in cells utilizing the alternative lengthening of telomeres (ALT) pathway. Life (Basel) *11* (*278*), 1–16.

Vannier, J.B., Pavicic-Kaltenbrunner, V., Petalcorin, M.I., Ding, H., and Boulton, S.J. (2012). RTEL1 dismantles T loops and counteracts telomeric G4-DNA to maintain telomere integrity. Cell *149*, 795–806.

Wang, Y., Yang, J., Wild, A.T., Wu, W.H., Shah, R., Danussi, C., Riggins, G.J., Kannan, K., Sulman, E.P., Chan, T.A., et al. (2019). G-quadruplex DNA drives genomic instability and represents a targetable molecular abnormality in ATRX-deficient malignant glioma. Nat. Commun. *10*, 943.

Ward, T.A., Dudasova, Z., Sarkar, S., Bhide, M.R., Vlasakova, D., Chovanec, M., and McHugh, P.J. (2012). Components of a Fanconi-like pathway control Pso2-independent DNA interstrand crosslink repair in yeast. PLoS Genet. *8*, e1002884.

Yang, Q., Zhang, R., Wang, X.W., Linke, S.P., Sengupta, S., Hickson, I.D., Pedrazzi, G., Perrera, C., Stagljar, I., Littman, S.J., et al. (2004). The mismatch DNA repair heterodimer, hMSH2/6, regulates BLM helicase. Oncogene *23*, 3749–3756.

Yang, S.Y., Chang, E.Y.C., Lim, J., Kwan, H.H., Monchaud, D., Yip, S., Stirling, P.C., and Wong, J.M.Y. (2021). G-quadruplexes mark alternative lengthening of telomeres. NAR Cancer *3*, zcab031.

Zhang, J.M., Yadav, T., Ouyang, J., Lan, L., and Zou, L. (2019). Alternative lengthening of telomeres through two distinct break-induced replication pathways. Cell Rep. *26*, 955–968.e953.

Zimmer, J., Tacconi, E.M., Folio, C., Badie, S., Porru, M., Klare, K., Tumiati, M., Markkanen, E., Halder, S., Ryan, A., et al. (2016). Targeting BRCA1 and BRCA2 deficiencies with G-quadruplex-interacting compounds. Mol. Cell *61*, 449–460.

STAR★METHODS

KEY RESOURCES TABLE

REAGENT or RESOURCE	SOURCE	IDENTIFIER
Antibodies		
Anti-TRF2, rabbit polyclonal	Santa Cruz	Cat# sc-9143, RRID:AB_2201333
Anti-TRF2, mouse monoclonal	Millipore	Cat# 05-521, RRID:AB_2303145
Anti-MSH2, rabbit polyclonal	Santa Cruz	Cat# sc-494, RRID:AB_631975
Anti-MSH3, rabbit polyclonal	Abcam	Cat# Ab154521 RRID: NotFound
Anti-GTBP (E-8), mouse monoclonal	Santa Cruz	Cat# sc-137015, RRID:AB_2144968
Anti-PML, rabbit polyclonal	Santa Cruz	Cat# sc-5621, RRID:AB_2166848
Anti-gamma H2AX, mouse monoclonal	Millipore	Cat# 05-636, RRID:AB_309864
Anti-53BP1, rabbit polyclonal	Santa Cruz	Cat# sc-22760, RRID:AB_2256326
Anti-BLM, rabbit polyclonal	Abcam	Cat# ab476, RRID:AB_304596
Anti-TFIIH, rabbit polyclonal	Santa Cruz	Cat# sc-293, RRID:AB_2262177
Anti-DNA/RNA G-quadruplex (BG4)	Absolute antibody	Cat# Ab00174-1.1 RRID: NotFound
Anti-DNA-RNA hybrid (S9.6), mouse monoclonal	Kerafast	Cat# ENH001, RRID:AB_2687463
Antibody conjugated with Alexa Fluor 488, anti-rabbit	Life Technologies	Cat# A-11008, RRID:AB_143165
Antibody conjugated with Alexa Fluor 568, anti-mouse	Life Technologies	Cat# A-11037, RRID:AB_2534095
Anti-MSH2, mouse monoclonal	Calbiochem	Cat# NA27, RRID:AB_2266524
Anti-Lamin B1 (S20), goat polyclonal	Santa Cruz	Cat# sc-30264, RRID:AB_2136305
Anti-GTBP (MSH6), mouse monoclonal	BDTransductionLab	Cat# 610919, RRID:AB_398234
Anti-BTBD12 (SLX4), mouse monoclonal	Abnova	Cat# H00084464-B01P, RRID:AB_1673069
Anti-XPF (SPM228), mouse monoclonal	Abcam	Cat# ab17798, RRID:AB_444016
Anti-MUS81, mouse monoclonal	Santa Cruz	Cat# sc-53382, RRID:AB_2147138
Anti-rabbit IgG Peroxidase-Conjugated	Sigma-Aldrich	Cat# A6667, RRID:AB_258307
Anti-mouse IgG Peroxidase-Conjugated	Sigma-Aldrich	Cat# A4416, RRID:AB_258167
Rabbit Anti-goat IgG Peroxidase-Conjugated	Dako	Cat# P0449, RRID:AB_2617143
Chemicals, peptides, and recombinant proteins		
Pyridostatin trifluoroacetate salt	Sigma-Aldrich	SML0678
Lipofectamine RNAiMAX Reagent	Invitrogen	13,778
Lipofectamine 2000 Reagent	Invitrogen	11,668
BLOCK-iT™ Inducible Pol II miR-RNAi Expression Vector Kit with EmGFP	Life Technologies	K4939-00
Protease inhibitors (Complete Mini EDTA-free cocktail tablets)	Roche	04693124001
Phosphatase inhibitors (Complete Mini EDTA-free cocktail tablets)	Roche	04906837001
ECL substrate	Thermo Scientific	1859698 & 1859701
DAPI	Sigma	D9542
Vectashield mounting medium with DAPI	Vector Laboratories	H-1200
Hoechst 33258	Sigma	B1155
KaryoMAX Colcemid	Gibco	15219-040
1x HOT FIREPol EvaGreen qPCR supermix	Solis BioDyne	08-36-00,001
BrdU	Sigma	B9285
RNase A	Sigma	R5000
RNase H	NEB	M0297S
Exonuclease III	Promega	M1811
*Hinf*I	Thermo scientific	ER1121
*Rsa*I	Thermo scientific	ER0801

(*Continued on next page*)

Continued

REAGENT or RESOURCE	SOURCE	IDENTIFIER
Phi29 DNA polymerase	Life Technologies	EP0092
PerfectHyb Plus hybridization buffer	Sigma-Aldrich	H7033
Klenow fragment 3'→ 5′ exo-	NEB	M0212S
Magnetic Dynabeads Protein G	Invitrogen	100-07D
Experimental models: Cell lines		
H.sapiens: U2OS	ATCC	HTB-96™
H.sapiens: Saos2	ATCC	HTB-85™
H.sapiens: WI-38 VA-13 (VA-13)	ATCC	CCL-75.1™
H.sapiens: HEK293	ATCC	CRL-1573™
H.sapiens: HeLa	ATCC	CCL-2™
H.sapiens: HeLa LT		(O'Sullivan et al., 2014)
H.sapiens: A172	ATCC	CRL-1620™
H.sapiens: U2OS T-REx GFP-RNaseH1 WT		(Teloni et al., 2019)
H.sapiens: U2OS MSH2-KO		This manuscript
Oligonucleotides		
gRNA MSH2-Ex1 F 5′-CACCGGAAGCGCACGAAGCCGACCT-3′	Tag Copenhagen	N/A
gRNA MSH2-Ex1 R 5′-AAACAGGTCGGCTTCGTGCGCTTCC-3′	Tag Copenhagen	N/A
miR-RNAi MSH2- top strand 5′ TGCTGTTGAACTTCAACACAAGCATGGTTTTGGCC ACTGACTGACCATGCTTGTTGAAGTTCAA 3′	Tag Copenhagen	N/A
miR-RNAi MSH2- bottom strand 5′ CCTGTTGAACTTCAACAAGCATGGTCAGTCAGTG GCCAAAACCATGCTTGTGTTGAAGTTCAAC 3′	Tag Copenhagen	N/A
miR-RNAi MSH3- top strand 5′ TGCT GATTTGAGAACCTTTGATGTCAGTTTTGGCC ACTGACTGACTGACATCAGGTTCTCAAAT 3′	Tag Copenhagen	N/A
miR-RNAi MSH3- bottom strand 5′ CCTGATTTGAGAACCTGATGTCAGTCAGTCAGTGG CCAAAACTGACATCAA AGGTTCTCAAATC 3′	Tag Copenhagen	N/A
miR-RNAi MSH6- top strand 5′ TGCTGAACAGATGACAAGATCAAAGTGTTTTGGC CACTGACTGACACTTTGATTGTCATCTGTT 3′	Tag Copenhagen	N/A
miR-RNAi MSH6- bottom strand 5′ CCTGAACAGATGACAATCAAAGTGTCAGTCAGTG GCCAAAACACTTTGATCTTGTCATCTGTTC 3′	Tag Copenhagen	N/A
siLUC (5′-CGUACGCGGAAUACUUCGAUU-3′)	Sigma-Aldrich	N/A
siMLH1 (5′-UCCACAAGUAUUCAAGUGA-3′)	Sigma-Aldrich	N/A
siMSH2 (5′-CUUGAGGAGUUUCAGUAUA-3′)	Sigma-Aldrich	N/A
siMSH3-1 (5′-GGAAUCUGGAAAUCCUACA-3′)	Sigma-Aldrich	N/A
siMSH3-2 (5′-CUAUACGCCGCUAGAAUUA-3′)	Sigma-Aldrich	N/A
siMSH3-3 (5′-UCGAGUCGAAAGGAUGGAUAA-3′)	Sigma-Aldrich	N/A
siMSH6 (5′-GUAAGUAUCUUCUUAGCCU-3′)	Sigma-Aldrich	N/A
siBLM (5′-CCGAAUCUCAAUGUACAUAGA-3′)	Sigma-Aldrich	N/A
siSLX4 (5′-GAGAAGAACCCUAAUGAAA-3′)	Sigma-Aldrich	N/A
siMUS81 (5′-GCCAUAUGUGUCAUGUAGATT-3′)	Ambion	AM16704
siXPF (5′-GUAGGAUACUUGUGGUUGA-3′)	Sigma-Aldrich	N/A
Tel G primer for qPCR: 5′ACACTAAGGTTTGGGTTTGGGTTTGGGTTTGGGTTAGTGT-3′	Tag Copenhagen	N/A

(*Continued on next page*)

Continued

REAGENT or RESOURCE	SOURCE	IDENTIFIER
Tel C primer for qPCR: 5′ GTTAGGTATCCCTATCCCTATCCCTATCCCTATCCC TAACA 3′	Tag Copenhagen	N/A
PNA probe TelC-Alexa 488	PNABio	F1004
PNA probe TelG-Cy3	PNABio	F1006
PNA probe CENPB-Cy3	PNABio	F3002
(CCCTAA)3 probe for C-circle assays	Tag Copenhagen	N/A
(TTAGGG)3 probe for TRF assays	Tag Copenhagen	N/A
G4T template 5′-TTTTTTTTTTTTGGGTGGGTGGGTG GGTTTTTTTTTTTTGGTAGAATTCGGCAGCGTC-3′	Microsynth	N/A
TAMRA 20 primer 5′ TAMRA- GA CGC TGC CGA ATT CTA CCA 3′	Microsynth	N/A
G3T 5′ TAMRA-GGGTGGGTGGGTGGGT 3′	Microsynth	N/A

RESOURCE AVAILABILITY

Lead contact

Further information and requests for resources and reagents should be directed and will be fulfilled by the lead contact, Javier Peña-Diaz (jdiaz@sund.ku.dk).

Materials availability

This study did not generate new unique reagents. Cell lines generated in this paper are available from the lead contact upon request.

Data and code availability

- All data reported in this paper will be shared by the lead contact upon request.
- This paper does not report original code.
- Any additional information required to reanalyze the data reported in this paper is available from the lead contact upon request.

EXPERIMENTAL MODEL AND SUBJECT DETAILS

Cell lines and cell culture

U2OS, U2OS MSH2-KO, Saos2, WI-38 VA-13, HEK293, HeLa, HeLa LT (O'Sullivan et al., 2014) and A172 cells were cultured in DMEM-Glutamax (Life Technologies) supplemented with 10% fetal bovine serum and 1% penicillin-streptomycin. Cells were cultured at 37°C and 5% CO2. U2OS T-REx cell lines carrying a pAIO vector for the expression of RNase H1/GFP was cultures in DMEM supplemented with 10% fetal calf serum (Tet-free approved), 100U/ml penicillin, and 100 μg/mL streptomycin, 50 μg/mL hygromycin B and 1 μg/mL puromycin (Chappidi et al., 2020). Doxycycline (1 ng/mL) was added for 24 h to induce the expression of recombinant RNase H1. U2OS MSH2-KO cells were generated using CRISPR-Cas9 technology as described elsewhere (Ran et al., 2013). Briefly, gRNAs targeting exon 1 of MSH2 were designed using the CRISPRdirect software (Naito et al., 2015). The gRNAs used to generate the plasmids are listed in the Key resources table. The gRNAs were cloned into the pSpCas9(BB)-2A-GFP vector for co-expression with Cas9. Cells were seeded at 0.3x106 cells/well in 6-well dishes. After 24 h, cells were transfected with sequenced-verified gRNAs cloned into pSpCas9(BB)-2A-GFP vector (1.25 μg DNA/well) using Fugene (Promega). 24 h after transfection, GFP-positive single cells were sorted into a 96-well plate using a FACS Aria-II cells sorter (BD Biosciences). Clones were expanded for 2 weeks and screened by Western blot analysis using MSH2 antibodies. Clone #4 lacking MSH2 expression was chosen for further analysis.

METHOD DETAILS

Small interference RNA transfections and treatment

For siRNA transfection, cells were seeded in DMEM complete medium to reach a confluency of 30%–40% at the day of transfection. Transfections of siRNAs at a final concentration of 40 nM were done using Lipofectamine RNAiMAX according to the manufacturer's instructions. 24 h after siRNA transfection, cells were trypsinized and re-seeded. Cells were harvested 72 h after transfection. Treatments with 0.2–2 μM Pyridostatin were performed 72 h after transfection for 3 h, as indicated sequences of siRNAs used are shown in the Key resources table.

Inducible knockdown of gene expression

To investigate the long-term effects of MMR protein depletions on telomere dynamics, we generated miR-RNAi that target and silence specific MMR genes with sustainable effects. We used the BLOCK-iT™ Inducible Pol II miR-RNAi Expression Vector Kit with EmGFP, which combines BLOCK-iT™ RNAi and T-REx™ technologies, to facilitate doxycycline-regulated expression of the miRNA of interest from a Pol II/TO RNAi cassette for use in RNA interference (Guberman et al., 2011) analysis in mammalian cells. The DNA oligonucleotides encoding the pre-miRNA of MSH2, MSH3 and MSH6 are listed in the Key resources table. To generate stable cell lines harbouring this inducible system, U2OS cells were transfected with BLOCK-iT™ Inducible Pol II miR-RNAi Expression Vector entry construct using Lipofectamine 2000 Reagent according to the manufacturer's instructions. miR-RNAi transfected U2OS cells were cultured in DMEM-Glutamax supplemented with 10% Tet System approved fetal bovine serum (Clontech) and 1% penicillin-streptomycin and selected in the presence of 5 μg/mL Geneticin Sulfate (G418) and 200 μg/mL Blasticidin. Addition of 50 ng/mL doxycycline was used to induce the expression of the miRNA of interest. Clones were generated from single cells and knockdown efficiency assessed by western blot analysis.

Western blotting

In order to obtain total protein extracts, cells were lysed using either Laemmli lysis buffer (4% SDS, 20% glycerol, 120 mM Tris-HCl, pH 6.8) or RIPA buffer (150 mM NaCl, 1.0% IGEPAL® CA-630, 0.5% sodium deoxycholate, 0.1% SDS, and 50 mM Tris-HCl, pH 8.0) supplemented with protease and phosphatase inhibitors and denatured for 10 min at 70°C. In order to prepare chromatin enriched protein fractions, cells were incubated with Pre-extraction Buffer (0.025 M HEPES-NaOH, pH 7.4, 0.05 M NaCl, 1 mM EDTA, 3 mM $MgCl_2$, 0.3 M Sucrose, 0.5% Triton X-100) supplemented with protease inhibitors for 10 min on ice prior to lysis. Proteins were resolved by SDS-PAGE using NuPage 4–12% Bis-Tris 1 mm gel and NuPage MOPS SDS buffer (Invitrogen), at 200 V for 1 h. Proteins were transferred to PVDF membrane by semidry transfer for 1 h and 10 min at 65 mA. Membranes were blocked in 5% milk or BSA in TBS-0.1% Tween 20 for 30 min, and incubated with primary antibodies overnight at 4°C and secondary antibodies for 1 h at RT. Antibodies used are listed in the Key resources table. Primary antibodies were used at a dilution 1:1000 unless otherwise stated, while secondary antibodies were used at a dilution 1:5000. The signal was visualized with ECL substrate in an Amersham imager 600 (GE Healthcare).

Immunofluorescence assays

Cells were washed twice in PBS and fixed with 4% formaldehyde in PBS for 10 min at RT. Formaldehyde was washed off with PBS thrice. Cells were permeabilized with 0.2% (v/v) Triton X-100 in PBS for 5 min and incubated with blocking solution (DMEM/5%FBS/0.05% Sodium Azide or PBS/2.5% BSA) for 30 min at RT. Primary antibodies were diluted in blocking solution and added to the cells for 2 h at RT or overnight at 4°C. Cells were washed twice with PBS/0.1% Tween 20 and incubated with secondary antibodies conjugated with Alexa Fluor for 1 h at RT. Antibodies were washed off with PBS/0.1% Tween 20. Nuclei were stained with 250 ng/mL DAPI for 5 min at RT on 96-wells microplates (Greiner Bio One, ref: 655,040) or mounted on slides with Vectashield mounting medium with DAPI. Images were obtained with either LSM 710 confocal microscope by Carl Zeiss (Z stacks/colocalisation identification) or a motorized Olympus IX-81 wide-field microscope equipped with fast-switching filter wheels for excitation and emission of DAPI, FITC, Cy3, and Cy5 fluorescent dyes (foci quantification); an MT20 Illumination system; and a digital monochrome Hamamatsu C9100 CCD camera. An Olympus UPLSAPO 40×/0.9 NA objective was used. Automated unbiased image acquisition was carried out by the propriety ScanR acquisition software and analyses performed using the ScanR analysis software as previously described (Teloni et al., 2019; Toledo et al., 2013).

For detection of G4 by immunofluorescence, a previously described protocol was used (Biffi et al., 2013). Briefly, cells were washed in PBS and fixed in methanol/acetic acid (3:1) for 10 min on ice. Following washes with PBS, cells were permeabilized with 0.1% (v/v) Triton X-100 in PBS for 10 min on ice and incubated with 200 μg/mL RNase A in PBS for 1 h at RT. Then, cells were incubated with blocking solution (2% dry milk in PBS/0.1% Tween 20) for 30 min at RT. Primary antibodies were diluted in blocking solution and added to the cells for overnight incubation at 4°C. BG4 antibody was diluted to 1:500. Cells were washed three times with PBS/0.1% Tween 20 for 5 min and incubated with secondary antibodies conjugated with Alexa Fluor for 1 h at RT. Antibodies were washed off with PBS/0.1% Tween 20. Samples were mounted on slides with Vectashield mounting medium with DAPI and visualized in an automated upright microscope system with fluorescence illumination (Leica DM4B).

For detection of RNA:DNA hybrids by immunofluorescence, an alternative protocol was used. Briefly, cells were washed once with PBS, once with pre-extraction Buffer (0.025 M HEPES-NaOH pH 7.4, 0.05 M NaCl, 1 mM EDTA, 3 mM MgCl2, 0.3 M Sucrose, 0.5% Triton X-100, complete protease inhibitors), followed by 10 min incubation with pre-extraction Buffer on ice. Afterward, cells were washed once with pre-extraction Buffer, once with PBS and permeabilized with 0.5% (v/v) Triton X-100 in PBS for 5 min at RT. Control samples were then incubated with 2 μL RNase H and 10 μL RNase H buffer, diluted in distilled water to a final volume of 50 μL, for 40 min. All samples were then incubated with 1 mg/mL RNase A in PBS for 20 min at RT. Following washes with PBS, cells were fixed with 4% formaldehyde in PBS for 10 min at RT. Formaldehyde was washed off by three washes with PBS. Primary antibodies were diluted in PBS and added to the cells for 2 h at RT or overnight at 4°C. S9.6 antibody was diluted to 1:250. Cells were washed three times with PBS/0.01% Tween 20 for 5 min and incubated with Alexa Fluor conjugated secondary antibodies for 1 h at RT. Antibodies were washed off with PBS/0.1% Tween 20. Samples were mounted on slides with Vectashield mounting medium with DAPI and visualized in an automated upright microscope system with fluorescence illumination (Leica DM4B). Antibodies used for immunofluorescence staining are listed in Key resources table and employed at a dilution 1:1000 unless otherwise stated.

Fluorescent *in situ* hybridization (FISH)

Cells grown either in slides or in cell culture microplates (PerkinElmer Cell carrier™ 96 ultra, ref:6,055,300) were washed twice in PBS and fixed with 4% formaldehyde for 10 min at RT. Formaldehyde was washed off with PBS thrice. Cells were permeabilized with 0.2% (v/v) Triton X-100 in PBS for 10 min, incubated with 0.1 M HCl for 15 min at RT followed by incubation with denaturing buffer (60% formamide, 2x SSC) for at least 30 min at RT. PNA probes, C-Tel-Alexa 488 and CENPB-Cy3, used are shown in the Key resources table. Prior to hybridization, the PNA probes were denatured at 55°C for 5 min and the hybridization solution (70% formamide, 25 mM MgCl2, 10 mM Tris-HCl, pH 7.5) preheated for 5 min at 85°C. Hybridization solution containing 1 ng/μL of 50 μM C-Tel-Alexa488 and 1 ng/μL of 50 μM CENPB-Cy3 was then added to the cells and incubated for 7 min at 85°C and then left to cool down for 2 h at RT in the dark. Cells were washed three times with 2x SSC, 0.1% Tween 20 for 10 min at 42°C, followed by three washes with 1x SSC. Finally, cells were incubated with 250 ng/mL DAPI for 5 min at RT. Nuclei and metaphase chromosomes were visualized by high throughput-high content microscopy (Olympus IX-81) and confocal microscopy (LSM 710, Carl Zeiss).

Metaphase chromosome spreads

U2OS cells were incubated with 0.1 μg/mL KaryoMAX Colcemid for 1.5 h at 37°C, 5% CO_2 and 95% humidity. Then, cells were harvested and incubated with preheated hypotonic solution (75 mM KCl) at 37°C for 20 min. Cells were fixed with methanol: acetic acid (3:1) at RT. Samples were kept at −20°C until further analysis. Metaphase chromosomes were spread by dropping the mixture onto slides/coverslips.

Chromosome orientation FISH (CO-FISH)

Cell cultures were incubated with 5 μg/mL BrdU for 22 h. Cells were washed to remove BrdU and colcemid was added for an additional 1.5 h. Cells were harvested and fixed as described above and metaphase chromosomes were spread on coverslips. Samples were rehydrated in PBS for 5 min at RT and then treated with 0.5 mg/mL RNase A for 15 min at 37°C. Coverslips were incubated in 10 μg/mL Hoechst 33,258 for 15 min at RT in the dark and irradiated for 20 min (5.4×10^5 J/m^2) under 365 nm UVP Minerlight Lamp (model UVGL-58, UVP). McIlvaines Buffer was used to prevent coverslip drying during irradiation. The nicked BrdU-substituted DNA strands were degraded using 3 U/μl of Exonuclease III in the buffer supplied by the manufacturer at RT for 10 min. The coverslips were washed in PBS for 5 min and kept in the denaturation buffer (60% formamide, 2x SSC) for at least 30 min at RT. Prior to hybridization, PNA probe TelC-Alexa 488 was denatured at 55°C for 5 min and the hybridization solution (70% formamide, 25 mM $MgCl_2$, 10 mM Tris-HCl, pH 7.5) preheated for 5 min at 85°C. Cells were washed five times with 2x SSC for 10 min at 42°C, gently rocking and then TelG-Cy3 PNA probe was added and incubated for 2 h at RT in the dark. The coverslips were washed five times with 2x SSC for 10 min at 42°C and then were mounted with Vectashield mounting medium with DAPI. PNA probes TelC-Alexa 488 and TelG-Cy3 used are shown in the Key resources table. Leading and lagging strand of metaphase chromosomes were visualized by confocal microscopy (LSM 710, Carl Zeiss).

Rolling circle amplification assay

The protocol for C-circle amplification was developed by Reddel's group (Henson et al., 2009). Briefly, genomic DNA was purified and digested with 4 U/μg DNA *Hinf*I and *Rsa*I restriction enzymes in the presence of 25 ng/μL RNase A at 37°C overnight. Concentration of digested DNA was measured and diluted up to 10 ng/μL in Tango Buffer. 50 ng of digested DNA were mixed with 0.2 μg/μL BSA, 0.1% Tween 20, 1 mM each dATP, dTTP, dGTP and 1x Phi29 buffer in the presence or absence of 7.5 U Phi29 DNA polymerase in a volume of 20 μL. Samples were incubated at 30°C for 4 h followed by incubation at 65°C for 20 min. Reaction products were diluted to 166 μL with 2x SSC and dot-blotted onto a 2x SSC-soaked nylon membrane. DNA was UV cross-linked on the membrane (2600 x100 μJoules, 120 mJ/cm^2) in a UV Stratalinker 2400 (Stratagene) and hybridized with a ^{32}P-labelled $(CCCTAA)_3$ telomeric probe diluted in PerfectHyb Plus hybridization buffer at 37°C overnight. Blots were washed thrice for 30 min each at 37°C in 0.5x SSC/0.1% SDS pre-warmed buffer, exposed to PhosphoImager screens, scanned and visualized using Typhoon 9400 PhosphoImager (GE Healthcare).

G-quadruplex biochemical assays

MutSβ heterodimers carrying a hexahistidine tag on MSH3 were produced in Sf9 insect cells by means of baculovirus system and purified as previously described (Burdova et al., 2015). Protein dilutions were performed in buffer containing 50 mM Tris-HCl (pH 7.5), 0.2 M NaCl, 1 mM DTT and 0.1 mM EDTA.

The oligonucleotides, G4T template, TAMRA 20 primer and G3T, used are listed in the Key resources table. The oligonucleotides were heat denatured at 95°C for 10 min followed by slow cooling to RT to allow annealing and/or formation of G4 structures. The annealing buffers employed (10 mM Tris-HCl, pH 8, 0.5 mM EDTA) either did not contain salts or contained 50 mM KCl or 50 mM NaCl. The final oligonucleotide concentrations in the annealing reaction were of 250 nM for the TAMRA-tagged primers and 450 nM for the G4T template used for annealing with the primer TAMRA 20.

G-quadruplex binding assays were performed using a reaction mixture (10 μL) containing 0.05 mg/mL BSA, 10 mM Tris-HCl, pH 8, 1 mM DTT, 50 mM NaCl, 10 mM $MgCl_2$, the indicated concentrations of MutSβ and 100 nM DNA substrate. The reactions were incubated for 10 min at RT before adding loading buffer (10 μL) containing 30% glycerol, 0.05 mg/mL BSA, 10 mM Tris-HCl, pH 8, 1 mM

DTT, 50 mM NaCl, 2 mM ATP, 10 mM $MgCl_2$. The reaction mixtures were loaded onto a 6% native acrylamide and run in 1xTBE buffer at 100 Volt for 6 h. Gels were imaged using a Typhoon 9410 (GE Healthcare).

G-quadruplex stability assays were performed using a reaction mixture (10 μL) containing 0.05 mg/mL BSA, 10 mM Tris-HCl, pH 8, 1 mM DTT, 50 mM NaCl, 2mM ATP, 10 mM $MgCl_2$, MutSβ at concentrations of 5, 10, 20 and 40 nM and 25 nM DNA substrate. The reaction mixtures were incubated for 10 min at 37°C before adding Klenow reaction mixture (10 μL) containing 0.05 mg/mL BSA, 10 mM Tris-HCl, pH 8, 1 mM DTT, 50 mM NaCl, 10 mM $MgCl_2$, 0.1 mM dNTPs and with or without 0.05 U of Klenow fragment 3'→5′ exo-. This mixture was incubated for 30 min at 37°C before adding denaturing loading buffer (20 μL) containing 95% formamide, 50 mM EDTA and 0.02% bromophenol blue. The mixture was incubated at 95°C for 10 min prior to loading onto a 12% denaturing urea polyacrylamide gel. Electrophoresis was performed in 1x TBE buffer at 400 V. Gels were imaged using a Typhoon 9410 (GE Healthcare).

Terminal restriction fragment assay (TRF)

TRF analysis was performed essentially as described previously (Perrem et al., 2001). Briefly, genomic DNA was purified and digested with 4 U/μg DNA HinfI and RsaI restriction enzymes in the presence of 25 ng/μg RNase A at 37°C overnight. The digested DNA was loaded and run on 0.8% (w/v) agarose gel in 0.5x TBE buffer at 60 V (2 V/cm) for 14 h at 4°C. DNA was depurinated by immersing the gel into depurination solution (0.25 M HCl) for 30 min, followed by denaturation (0.5 M NaOH/1.5 M NaCl) and neutralization (1.5 M NaCl/0.5 M Tris) for 30 min each. DNA was transferred to nylon membranes (GeneScreen Hybridization Transfer Membrane, PerkinElmer, NEF1018001PK) soaked in 2x SSC according to the Southern blotting assay as previously described (Kimura et al., 2010). DNA was cross-linked by UV irradiation onto the membrane (1200 x100 μJoules) in a UV Stratalinker 2400 (Stratagene) and hybridized with a ^{32}P-labelled (TTAGGG)3 telomeric probe diluted in PerfectHyb Plus hybridization buffer at 37°C overnight. The membrane was washed thrice in 0.5x SSC/0.1% SDS pre-warmed buffer for 30 min each at 37°C, exposed to PhosphoImager screens, scanned and visualized using Typhoon 9400 (GE Healthcare).

Detection of R-loops at telomeres by DNA:RNA hybrid immunoprecipitation (DRIP) followed by qPCR

DRIP-qPCR was carried out essentially as described previously (Boque-Sastre et al., 2017). Briefly, cells were lysed in DRIP lysis buffer (0.5% SDS, 50 mM Tris-HCl, pH 7.5, 20 mM EDTA; 500 μL lysis buffer per 107 cells) and incubated with 200 ng/μL Proteinase K for 4 h at 37°C. Then, 5M NaCl was added to the mixture to a final concentration of 1.5 M and spun down at 20,000 x g for 15 min. DNA was isolated by ethanol precipitation. Genomic DNA (50 μg) was digested with 1 U/μg DNA *Hinf*I and *Rsa*I restriction enzymes at 37°C overnight. Digested DNA was then sonicated for 4 min (in total): pulse, 1 s ON, 1 s OFF, total ON 2 min, with an amplitude of 20% in ice-cold water bath using a Branson Digital Sonifier SFX250. Half sample volume was transferred into a new tube and incubated with 25 U (1.25 U/μg) RNase H for 2 h at 37°C. Samples treated with RNase H were used as negative control. DNA from all samples was collected by phenol:chloroform extraction and ethanol precipitation and resuspended in 50 μL IP buffer [0.05% (v/v) Triton X-100 in PBS]. Digestion and sonication efficiency were verified by electrophoresis of 2 μL of DNA on 0.8% agarose gel. Approximately 10 μg of DNA and 5 μg of the S9.6 antibody were used per sample, and 500 ng of the same DNA were kept to be used as input material. Immunoprecipitation was performed using magnetic Dynabeads Protein G following the instructions given by the manufacturer. In order to elute the DNA, the beads were incubated for 3 h at 50°C with 2 μL Proteinase K diluted in 48 μL of TE buffer. Then, the samples were denatured in 0.4 M NaOH/10 mM EDTA and retrieved from the beads. The retrieved fragments were then analysed by qPCR using TelG and TelC primers (Cawthon, 2009) enlisted in the Key resources table. We employed 25 ng of input or 50–250 ng of immunoprecipitated DNA that were mixed with 250 nM telomere primers and 1x HOT FIREPol EvaGreen qPCR supermix. Amplification of the telomeric sequences was performed in a StepOnePlus Real-Time PCR System (Applied Biosystems) using 40 cycles of 15 s denaturation at 95°C, 30 s of annealing at 62°C and 20 s of extension at 72°C. Analysis was done on StepOne software v2.3 using the ΔCt method. Each sample was normalised first according to the negative qPCR control, to remove primers' background, and then according to the reference sample (siLUC untreated). The equations that we used are: ΔCT = (neg ctrl – sample) and ΔΔCT = (ΔCT of immunoprecipitated or input sample – ΔCT of reference immunoprecipitated or input sample). The fold increase was calculated as 2ΔΔCT and normalised by dividing each immunoprecipitated sample with its input.

DRIP-qPCR for Figures S7A and S7B was carried out essentially as previously described (Garcia-Rubio et al., 2018) with the inclusion of a sonication step (5 min, 1 s ON, 1 s OFF) using a Diagenode bioruptor sonication device.

QUANTIFICATION AND STATISTICAL ANALYSIS

Statistical comparisons were carried out in the GraphPad Prism 7.0 software, using the Mann-Whitney test method of significance for large datasets. For small datasets ($n \geq 3$) we used Student's t-test. All experiments were performed at least in triplicates and plotted as mean ± SD, unless stated otherwise.